Tailoring Green Silver Nanoparticles via Zingiberales Metabolomics: From Molecular Capping Architecture to pH- Triggered Therapeutic Response

Seyed Mohammad Faghih

sm.faghih@iau.ac.ir

Department of Chemical Engineering, So.C., Islamic Azad University, Sousangerd, Iran.

Najim Obaid Dawood

English Department, Al Nisour University, Baghdad, Iraq.

Mazin Abdulhussein Beden

University of Basrah Marine Science Center

Research Article

Keywords: Green synthesis, Silver nanoparticles, LC–MS/MS metabolomics, Structure–activity relationship, pH-responsive release, Heliconia psittacorum, Sustainable Pharmacy, Green Nanotechnology

Posted Date: May 26th, 2026

DOI: https://doi.org/10.21203/rs.3.rs-9521168/v1

Additional Declarations: No competing interests reported.

Tailoring Green Silver Nanoparticles via Zingiberales Metabolomics: From Molecular Capping Architecture to pH-Triggered Therapeutic Response

Seyed Mohammad Faghih[*1], Najim Obaid Dawood[2], Mazin Abdulhussein Beden[3]

[1]Department of Chemical Engineering, So.C., Islamic Azad University, Sousangerd, Iran.
*Corresponding Author Email: sm.faghih@iau.ac.ir, ORCID: 0000-0002-1552-8591
[2]English Department, Al Nisour University, Baghdad, Iraq.
[3]University of Basrah Marine Science Center, Basrah, Iraq.

Abstract:

While plant-mediated green synthesis of silver nanoparticles (AgNPs) is well documented, establishing a definitive molecular-level structure–activity relationship (SAR) linking specific phytochemical capping ligands to stimuli-responsive biomedical behavior remains a critical knowledge gap in sustainable pharmacy. This study addressed this issue through a comparative metabolomic analysis of AgNPs synthesized using three *Zingiberales* species: *Alpinia calcarata*, *Elettaria cardamomum*, and *Heliconia psittacorum*. An optimized, low-energy protocol (0.1 mM $AgNO_3$, 60°C, surfactant-free) was employed to synthesize spherical nanoparticles adhering to the principles of green nanotechnology. Comprehensive LC–MS/MS fingerprinting of *H. psittacorum* revealed a distinct capping corona dominated by flavonoid glycosides and nitrogenous protoalkaloids, which directly dictated the nano-architecture. Consequently, *H. psittacorum*-AgNPs exhibited significantly refined core crystallite and morphological sizes (~20 nm) compared to terpenoid-rich extracts. Critically, this specific alkaloid-rich corona imparted smart, pH-responsive dissolution kinetics; in vitro release profiling demonstrated a pronounced shift from classical Fickian diffusion at physiological pH (48% release) to anomalous, erosion-mediated transport at tumor-mimetic acidic pH (81% release). This targeted ion release directly translated to superior biological efficacy: *H. psittacorum*-AgNPs exhibited potent bactericidal activity (MIC = 6.25–12.5 μg/mL) and highly selective anticancer toxicity against MCF-7 cells (IC_{50} = 32.8 μg/mL, Selectivity Index ≥ 6.1), driven by ROS-mediated mitochondrial dysfunction. By bridging phytochemical metabolomics with smart nanomaterial kinetics, this study leverages botanical biodiversity for the rational design of sustainable pharmaceutical nanocarriers with predictable and eco-friendly therapeutic outcomes.

Keywords: Green synthesis; Silver nanoparticles; LC–MS/MS metabolomics; Structure–activity relationship; pH-responsive release; *Heliconia psittacorum*; Sustainable Pharmacy; Green Nanotechnology

1. Introduction

The transition toward sustainable nanomanufacturing has intensified the search for eco-friendly synthetic protocols that eliminate hazardous byproducts while preserving the functional efficacy of nanomaterials. (Ilavenil et al., 2025; Sati et al., 2025). Conventional chemical routes for synthesizing silver nanoparticles (AgNPs) typically rely on toxic reducing agents, synthetic surfactants, and high-energy inputs (often >90 °C), compromising their biocompatibility and contradicting the core principles of green chemistry (Ahmed et al., 2016; Fahim et al., 2024). In response, plant-mediated green synthesis has emerged as a highly viable alternative, utilizing aqueous botanical extracts as natural and benign reactors (Iravani, 2011). Beyond environmental remediation, these biogenic AgNPs hold immense therapeutic promise, particularly for combating multidrug-resistant pathogens and selectively targeting malignant cells via reactive oxygen species (ROS) generation and mitochondrial disruption (Ansar et al., 2020; More et al., 2023).

In green synthesis protocols, the aqueous plant extract is not merely a reducing agent; its complex mixture of secondary metabolites—forming a "phytochemical corona"—dictates the physicochemical destiny of the nanoparticle (Bhattacharjee, S.,2016; Park et al., 2011). Specifically, the molecular identity of this corona (composed of phenolics, flavonoids, terpenoids, and alkaloids) governs crystallite size, colloidal stability, and critically, the pH-dependent dissolution kinetics of silver ions (Ag^+) in acidic microenvironments (Bélteky et al., 2019; Miranda et al., 2022). The order Zingiberales represents a phytochemically diverse botanical reservoir for exploring these structure–activity relationships (Richards et al., 2015). Species within the Zingiberaceae family, such as *Alpinia calcarata* and *Elettaria cardamomum*, are well-documented sources of terpenoids and flavonoids that efficiently cap AgNPs (Alolga et al., 2022; Velmurugan et al., 2014). In contrast, *Heliconia psittacorum* (Heliconiaceae) possesses a distinct phytochemical profile rich in nitrogenous protoalkaloids and glycosides—chemical features theorized to modulate strongly Ag^+ release kinetics, yet this genus remains largely unexplored in green nanotechnology.

Despite the growing number of reports on Zingiberales-derived AgNPs, existing studies exhibit critical gaps that limit their translation into sustainable nanomedicine applications. First, comparative phytochemical analyses across different families within this order are limited. Second, and most importantly, prior studies have predominantly relied on qualitative colorimetric assays, failing to employ untargeted metabolomics (e.g., LC–MS/MS) to establish a definitive molecular-level structure–activity relationship (SAR) linking specific capping

ligands to nanoparticle performance(Fahim et al., 2024; Raza et al., 2023). Furthermore, the influence of this corona chemistry on pH-triggered Ag^+ release, a critical parameter for reducing systemic toxicity in nanopharmaceutical applications, has not been investigated for Zingiberales species. Without an integrated framework connecting the phytochemical fingerprint, nanoparticle structure, pH-responsive kinetics, and biological efficacy, the rational design of plant-based nanomaterials remains empirical.

The present study addresses these gaps through a systematic, green chemistry-driven comparative analysis of AgNPs synthesized from three *Zingiberales* species: *A. calcarata*, *E. cardamomum*, and *H. psittacorum*. Utilizing an optimized, low-energy aqueous protocol (60 °C, surfactant-free), the synthesis was designed in strict accordance with the principles of Green Chemistry, specifically emphasizing atom economy, energy efficiency, and the use of benign solvents. Following comprehensive characterization (UV–Vis, FTIR, SEM/EDX, TEM, XRD, DLS), this work integrates LC–MS/MS-based phytochemical fingerprinting with in vitro pH-dependent release profiling (pH 7.4 vs. 5.5) to construct a mechanistic SAR framework. We demonstrate how specific metabolites govern nano-architecture and how alkaloid-rich coronas facilitate stimuli-responsive release, driving ROS-mediated antibacterial and anticancer efficacy. This study provides the first mechanistic metabolomic insight into *Heliconiaceae*-derived AgNPs, highlighting their potential as sustainable pharmaceutical nanocarriers with predictable therapeutic performance.

2. Materials and Methods

2.1. Materials and Green Synthesis Principles

Silver nitrate ($AgNO_3$, 99% purity) was obtained from HiMedia Laboratories (Mumbai, India). The compounds 3-(4,5-dimethylthiazol-2-yl)-2,5-diphenyltetrazolium bromide (MTT), dimethyl sulfoxide (DMSO, ≥99.9% purity), and camptothecin (CPT, 95% purity) were sourced from Sigma-Aldrich (St. Louis, MO, USA). All other reagents were of analytical grade. To strictly adhere to green chemistry principles and avoid ionic interference during nanoparticle nucleation, all aqueous solutions were prepared using deionized water (Milli-Q system, resistivity >18 MΩ·cm) without the addition of any synthetic surfactants or stabilizers (Matyushov, 2024; Smith et al., 2017). Pathogenic bacterial strains (Pseudomonas aeruginosa ATCC 27853, MRSA ATCC 43300, Escherichia coli ATCC 25922, and Klebsiella pneumoniae ATCC 700603) and cell lines (MCF-7 and HEK-293) were obtained from American Type Culture Collection (ATCC, Manassas, VA, USA).

2.2. Plant Collection and Sustainable Extract Preparation

Fresh leaves from three Zingiberales species—Alpinia calcarata and Elettaria cardamomum (Zingiberaceae) and Heliconia psittacorum (Heliconiaceae)—were collected from the Botanical Garden of the University of Calicut, Kerala, India (Permit No. CUBG-2023-045). Botanical identities were confirmed by Dr. A. K. Pradeep, with voucher specimens deposited (UOC-BOT-5678 to -5680, respectively). Leaves were rinsed, shade-dried at 25 ± 2°C for 10 days to prevent thermal degradation of heat-sensitive metabolites, and ground into a fine powder(Ahmed et al., 2016). Aqueous extracts were prepared at a sustainable 1:100 w/v ratio (1 g powder in 100 mL deionized water).

The mixtures were incubated in an orbital shaker at 60°C and 150 rpm for 24 h (Getachew et al., 2022). Although shade-drying at ambient temperature (25 ± 2°C) was employed to prevent irreversible thermal denaturation of proteins and volatile secondary metabolites during prolonged drying, aqueous extraction at 60°C represents a short, controlled thermal event (24 h in the liquid phase) that selectively solubilizes non-volatile thermostable phenolics, flavonoids, and alkaloids without inducing the structural degradation associated with dry-heat exposure above 70°C (Ongtanasup et al., 2024). The suspensions were filtered (Whatman No. 1), centrifuged (5000 × g), and freeze-dried to produce crude extract powders. The lyophilization yields were 18.2%, 16.5%, and 20.1% for A. calcarata, E. cardamomum, and H. psittacorum, respectively. Stock solutions (10 mg/mL in deionized water) were sterilized (0.22 μm) and stored at 4°C for up to 2 weeks (Table 1).

Table 1. Preliminary Phytochemical Analysis and Extraction Yield of Zingiberales Leaf Extracts

Parameter	A. calcarata Extract	E. cardamomum Extract	H. psittacorum Extract
Extraction Yield (w/w)	18.2%	16.5%	20.1%
Visual Color of Extract	Pale Yellow	Yellowish Green	Pale Yellow
Dominant Phytochemicals	Flavonoids & Terpenoids	Terpenoids & Gingerols	Protoalkaloids & Glycosides
Primary Capping Agents	Phenolics/Flavonoids	Phenolics/Flavonoids	Alkaloids & Flavonoids

2.3. Phytochemical Fingerprinting by LC–MS/MS

To establish a precise structure–activity relationship (SAR) and identify the bioactive metabolites responsible for the bioreduction and stabilization of AgNPs, metabolomic profiling

of H. psittacorum aqueous extract was performed. While preliminary phytochemical screening was conducted for all three species (Table 1), detailed LC–MS/MS analysis focused on H. psittacorum because of its superior nanoparticle performance, thereby enabling targeted elucidation of the molecular capping mechanism (Raza et al., 2023).

The extract was filtered through a 0.22 μm PTFE membrane and analyzed using an Agilent 1260 Infinity LC system coupled with a 6460 Triple Quadrupole Mass Spectrometer (Agilent Technologies, USA) equipped with an electrospray ionization (ESI) source. Chromatographic separation was achieved using a Zorbax Eclipse Plus C18 column (150 mm × 4.6 mm, 5 μm) maintained at 30°C. The mobile phase consisted of (A) 0.1% formic acid in deionized water (Milli-Q, resistivity >18 MΩ·cm) and (B) LC-MS grade acetonitrile. Linear gradient elution was applied as follows: 5–95% B over 25 min, followed by a 5 min re-equilibration step at a constant flow rate of 0.5 mL/min .

Mass spectra were acquired in both positive and negative ESI modes over the m/z range 50–1000. The capillary voltage was set at 3.5 kV, with a gas temperature of 300°C and a nitrogen drying gas flow of 10 L/min. Collision-induced dissociation (CID) was performed using nitrogen as the collision gas at 35 eV collision energy. The compounds were tentatively identified by comparing their accurate masses, retention times, and characteristic MS/MS fragmentation patterns with those in standardized databases, including METLIN, NIST, and PubChem (match scores> 80%). This comprehensive fingerprinting enabled the molecular-level identification of capping ligands, which were subsequently correlated with crystallite size, colloidal stability, and pH-responsive dissolution kinetics (Sections 3.2 and 3.3) (Fahim et al., 2024; Sati et al., 2025).

2.4. Biogenic Synthesis and Optimization of AgNPs

Green synthesis was initiated by adding 1 mL of plant extract stock (10 mg/mL) to 9 mL of aqueous $AgNO_3$ (0.1 mM) in a sterile flask (1:9 v/v ratio) and maintaining an initial pH of 7.0. The $AgNO_3$ concentration (0.1–2.0 mM) and temperature (25–60°C) were systematically optimized. Higher precursor concentrations caused SPR peak broadening and aggregation, while 60°C yielded the narrowest SPR peak in the shortest time without degrading phytochemicals (Dutta et al., 2019; Edison & Sethuraman, 2012). Two controls were maintained: extract without $AgNO_3$ and $AgNO_3$ without extract. Following synthesis, the AgNPs were centrifuged (12,000 × g, 15 min) and washed three times with deionized water to

remove unreacted ions and unbound phytochemicals, in accordance with green purification protocols (Bélteky et al., 2019). The pellets were lyophilized for dry characterization or redispersed for colloidal studies.

2.5. Physicochemical Characterization

UV–Vis spectroscopy (300–800 nm) confirmed the presence of the SPR bands. FTIR (KBr pellet method, 400–4000 cm^{-1}) was used to identify functional group shifts between raw extracts and AgNPs to confirm capping (Zhou et al., 2020). XRD (Philips PW1730, Cu Kα, λ = 1.5406 Å) was used to determine the crystalline phases (JCPDS 04-0783). Morphology and elemental composition were assessed via SEM-EDX (ZEISS GeminiSEM 300), and particle size was quantified using ImageJ on >100 nanoparticles per sample (Kim et al., 2020). The hydrodynamic size, Polydispersity Index (PDI), and Zeta Potential were measured via DLS (Malvern Zetasizer Nano ZS) at 25°C (Bhattacharjee, 2016).

2.6. Antibacterial Activity Assay

Minimum Inhibitory Concentration (MIC) and Minimum Bactericidal Concentration (MBC) were determined using the broth microdilution method according to CLSI M07 (2020) guidelines (Clinical & Institute, 2020; Wiegand et al., 2008). AgNPs were serially diluted (100–0.78 µg/mL) in Mueller-Hinton Broth, inoculated with ~2.5×10^5 CFU/mL of bacterial suspension, and incubated at 37°C for 24 h. The MIC was defined as the lowest concentration that prevented visible turbidity (OD_{600}). MBC was determined by subculturing from clear MIC wells onto Nutrient Agar; bactericidal activity was defined as MBC ≤ 4 × MIC (Pankey & Sabath, 2004).

2.7. Anticancer Cytotoxicity and Mechanistic Studies

MCF-7 (breast cancer) and HEK-293 (normal kidney) cells were cultured in DMEM supplemented with 10% FBS and 1% penicillin-streptomycin at 37°C in a 5% CO_2 humidified incubator (Freshney, 2015). Cells were seeded in 96-well plates and, upon reaching 80% confluence, exposed to varying concentrations of AgNPs (12.5–200 µg/mL) for 48 h. Cell viability was assessed using the 3-(4,5-dimethylthiazol-2-yl)-2,5-diphenyltetrazolium bromide (MTT) colorimetric assay (Bahuguna et al., 2017; Mosmann, 1983). To rule out nanoparticle-dye optical interference, a critical validation step in green nanomedicine, cell-free AgNP

controls were run in parallel, and absorbance values were mathematically corrected to ensure accuracy(Murphy et al., 2022). The IC_{50} values were calculated via nonlinear regression analysis (sigmoidal dose-response) using GraphPad Prism 9.0 (Le Berre et al., 2022; Sebaugh, 2011).

Intracellular reactive oxygen species (ROS) levels were measured using the $\mathbf{2', 7'}$ -dichlorodihydrofluorescein diacetate (DCFH-DA) probe (10 μM). After 24 h of exposure to the IC_{50}concentration, fluorescence was quantified at Ex/Em 485/530 nm (Liu et al., 2019; Wang & Joseph, 1999). Mitochondrial membrane depolarization ($\mathbf{\Delta\Psi_m}$) was evaluated using the JC-1 ratiometric dye. The transition from red fluorescence (J-aggregates in healthy mitochondria) to green fluorescence (monomers in depolarized mitochondria) was quantified using the ImageJ software (Gooz & Maldonado, 2023).

2.8. In Vitro pH-Dependent Ag^+ Ion Release Study

The stimuli-responsive release of Ag^+The He rhM. Psittacorum-AgNPs were evaluated using the dialysis bag diffusion method) Bélteky et al., 2019 .(Dialysis membranes (MWCO 12–14 kDa) containing 5 mL of AgNP suspension (equivalent to 500 μg of total silver) were immersed in 100 mL of release medium (PBS, pH 7.4, or acetate buffer, pH 5.5). At predetermined intervals (0–72 h), 2 mL aliquots were withdrawn and replaced with fresh buffers. The cumulative release percentage$(R_n)$was calculated as:

$$R_n = \frac{V_0 C_n + \sum_{i=1}^{n-1} V_i C_i}{M_{total}} \times 100$$

Where V_0 is the total volume (100 mL) ,V_i is the aliquot volume (2 mL) ,Cn is the silver concentration at time n , and M_{total} is the initial silver mass. To determine the diffusion mechanism, the release data were fitted to the Korsmeyer-Peppas model:

$$\frac{M_t}{M_\infty} = kt^n$$

In this equation M_t/M_∞represents the fraction of silver released at time t ,k is the release velocity constant, and n is the diffusion exponent indicating the release mechanism (Raza et al., 2023; Singh et al., 2016).

2.9. Statistical Analysis

All biological and physicochemical experiments were performed in three independent biological assays (performed in triplicate). Quantitative data are expressed as mean ± standard deviation (SD), except for MIC and MBC values, which are reported as ranges or mean ± SD to reflect the discrete increments of the 2-fold serial dilution series, ensuring compliance with CLSI M07 reporting standards (Wiegand et al., 2008). Statistical comparisons for MIC, MBC, and IC_{50} values were conducted using One-way Analysis of Variance (ANOVA) followed by Tukey's honest significant difference (HSD) post hoc test (Nanda et al., 2021). A p-value of < 0.05 was considered statistically significant.

3. Results and Discussion

3.1. Optimization of the Green Synthesis Protocol

The transition from conventional chemical reduction to plant-mediated biosynthesis necessitates rigorous optimization of reaction parameters to ensure reproducibility, minimize energy consumption, and eliminate the need for toxic stabilizers (Ilavenil et al., 2025; Raza et al., 2023). In this study, the bioreduction of Ag^+ to Ag^0 was initially monitored by a visible color transition of the reaction mixture from colorless to yellowish-brown, driven by the excitation of surface plasmon resonance (SPR) (Edison & Sethuraman, 2012; Vanlalveni et al., 2021). To establish an eco-friendly synthesis framework, two critical parameters were systematically optimized: the precursor concentration and thermal energy input.

First, the concentration of $AgNO_3$ was evaluated over the range of 0.1-2.0 mM at a fixed temperature of 60 °C (Table S1, SI). Higher concentrations (1.0–2.0 mM) accelerated the initial color change but induced detrimental colloidal instability. UV–Vis spectroscopy revealed that increasing the precursor concentration resulted in a red shift of the λ_{max} and a broadening of the SPR peak (increased FWHM), which is a well-documented indicator of polydispersity and nanoparticle aggregation (Dutta et al., 2019; Mourdikoudis et al., 2018). Visual inspection confirmed severe precipitation at higher concentrations after 24 h. Consequently, a low concentration of 0.1 mM $AgNO_3$ was selected as the optimal precursor. This aligns with the principles of atom economy and waste minimization in green chemistry, as it maximizes the conversion of silver ions into stable nanoparticles, avoiding excess unreacted precursors that would require downstream remediation (Fahim et al., 2024; Sati et al., 2025).

Second, the thermal energy required for bioreduction was optimized by monitoring the SPR intensity at 0.1 mM $AgNO_3$ across four temperatures (25, 40, 50, and 60 °C). As illustrated in Fig. 1(a–f), a direct relationship was observed between temperature and bioreduction rate, consistent with Arrhenius kinetics. At room temperature (25 °C), the reaction was sluggish,

yielding a weak and broad surface plasmon resonance (SPR) band, indicative of incomplete reduction and heterogeneous nucleation (Getachew et al., 2022).

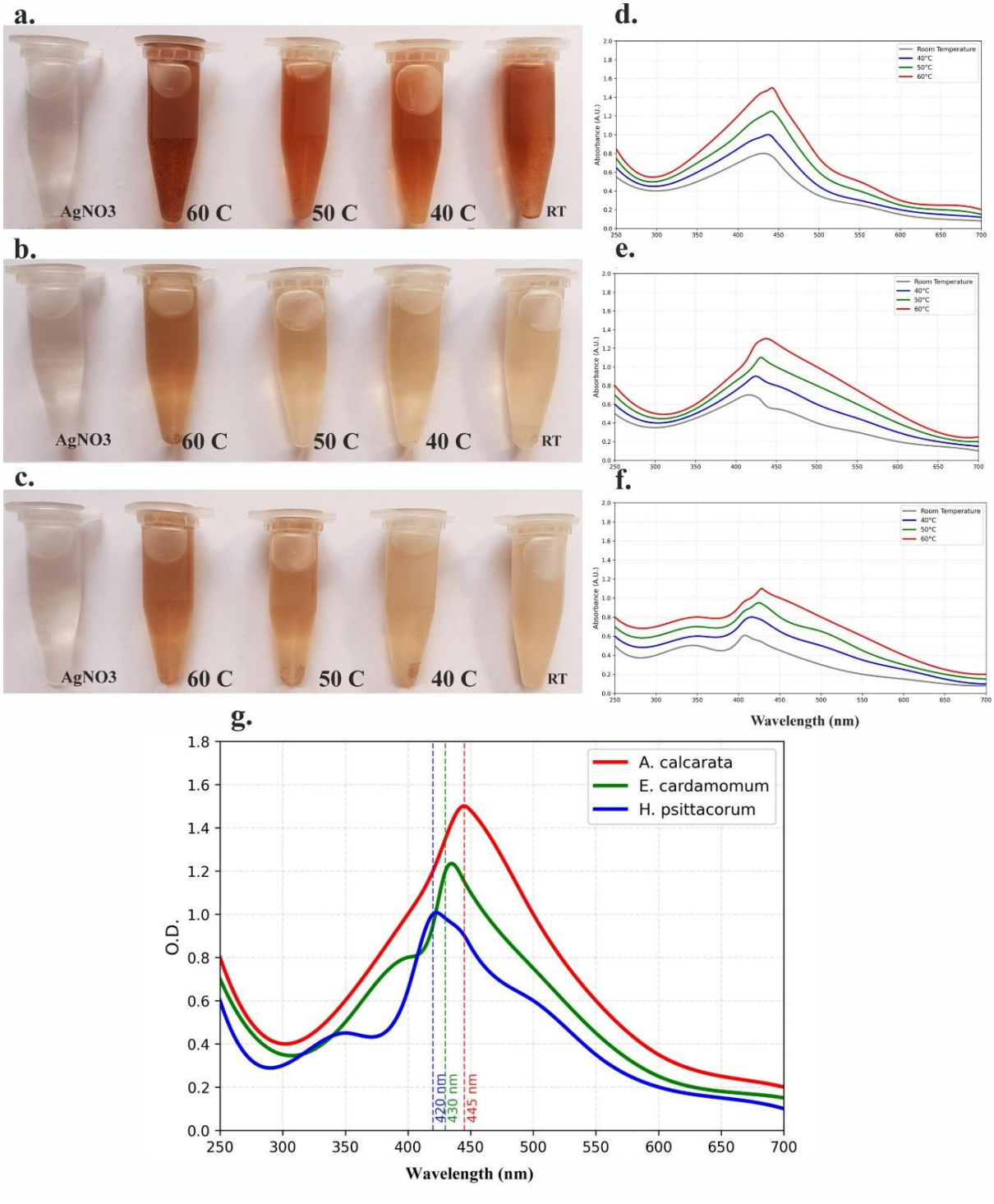

Fig. 1 Visual, spectroscopic, and kinetic tests confirmed the synthesis of silver nanoparticles (AgNPs) using a green method. They also determined the optimal reaction temperature. (a–c) AgNPs were synthesized over 2 h at different temperatures (60°C, 50°C, 40°C, and room temperature (RT)) using extracts from (a) A. calcarata, (b) E. cardamomum, and (c) H. psittacorum. The solution changed from clear to brown to yellow-brown, indicating the reduction of Ag^{+} ions. (d–f) UV–Vis absorption spectra showed that as the temperature increased, the surface plasmon resonance (SPR) peak became stronger and narrower for (d) A. calcarata, (e) E. cardamomum, and (f) H. psittacorum. The results showed that 60°C was optimal for AgNP production. (g) The final AgNPs prepared at 60°C exhibited different maximum absorbance (O.D.) and peak positions (λmax), indicating differences in

particle size and capping agent effectiveness. The λmax values were 445, 430, and 420 nm for A. calcarata, E. cardamomum, and H. psittacorum, respectively. The optimal $AgNO_3$ concentration was 0.1 mM, as determined by testing different concentrations (Table S1, SI).

Elevating the temperature to 60 °C resulted in a 1.8–2.3-fold increase in absorbance intensity ($p < 0.001$), producing the sharpest and most symmetrical SPR peak in the shortest reaction time (30–60 min). Notably, the final SPR peaks for the three plant extracts stabilized between 420 and 445 nm at 60 °C (Fig. 1g), confirming the formation of small, monodisperse spherical nanoparticles.

The selection of 60 °C as the optimal temperature represents a significant energy advantage over both conventional chemical methods and several recently reported green synthesis methods. For instance, the green synthesis of AgNPs using *Magnolia alba* required temperatures up to 95 °C to achieve adequate reduction (De Mel et al., 2025), while *Astragalus fasciculifolius* extracts required prolonged incubation times at room temperature, which can lead to larger, less uniform particles (Nosrati et al., 2025). The moderate thermal input of 60 °C utilized here provides an optimal energetic balance: it sufficiently accelerates the electron transfer from phytochemicals (phenols and flavonoids) to Ag^+ ions without inducing the thermal degradation of thermostable capping agents (Ongtanasup et al., 2024; Singh et al., 2016). Control experiments confirmed the necessity of both biological and metallic components, as neither the plant extract alone nor the AgNO3 solution exhibited characteristic SPR absorption. Together, the optimized parameters (0.1 mM AgNO3, 60 °C, aqueous solvent) establish a highly sustainable, low-energy, and surfactant-free protocol suitable for scaling-up biogenic AgNP production.

3.2. Phytochemical Profiling and Its Impact on Nanoparticle Architecture

A primary criticism of comparative green synthesis studies is their reliance on qualitative colorimetric assays to explain nanoparticle formation, which fails to establish a precise structure–activity relationship (SAR)(Raza et al., 2023). To address this, LC–MS/MS metabolomic profiling was conducted specifically on the *H. psittacorum* extract to identify the phytochemicals responsible for bioreduction and capping. As detailed in Table 2, the analysis revealed a distinct profile dominated by flavonoid glycosides (quercetin, quercetin-3-O-glucoside, and kaempferol) and nitrogen-containing protoalkaloids (e.g., m/z = 360.2).

The mechanistic roles of the identified compounds were corroborated by the FTIR spectral shifts observed before and after synthesis (Fig. 2). The broad O–H/N–H stretching vibration for he raw extract05 cm^{-1} in the rextract to 3425 cm^{-1} in the *H. psittacorum*-AgNPs,

accompanied by an approximate 35% reduction in intensity. This depletion confirms that the multiple hydroxyl groups of qquercetin and kaemferolact as primary electron donors for the reduction of superoxideinand kaemferolact as primary eelectron donorsfor the reduthe ction of Ag^{+} to Ag^{0} (Park et al., 2011; Singh et al., 2018). Concurrently, the C=O stretching band shifted from 1710 cm^{-1} to 1725 cm^{-1}, indicating the coordination of these oxidized flavonoid moieties to the nascent silver surface. The detection of protoalkaloids provides complementary evidence, as their strong affinity for metallic surfaces likely contributes to a robust capping corona that prevents uncontrolled crystal growth (Makarov et al., 2014; Bhattacharjee, S.,2016).

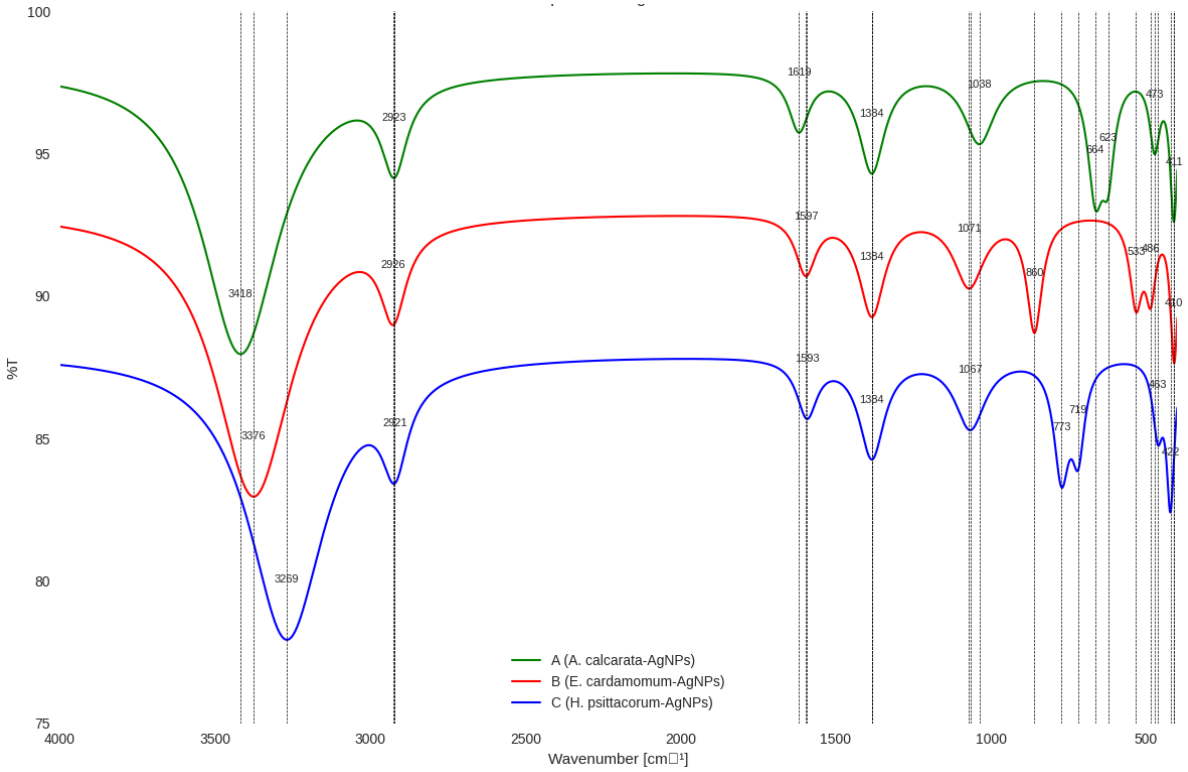

Fig. 2 Comparison of The Fourier-transform infrared (FTIR) spectra of silver nanoparticles (AgNPs) synthesized using three distinct plant extracts. The spectra (A. calcarata-AgNPs: red line; E. cardamomum-AgNPs: green line; H. psittacorum-AgNPs: blue line) confirm the involvement of phytochemical functional groups in the reduction of Ag+ ions and surface stabilization (capping) of nanoparticles. The observed shift and reduction in the intensity of key peaks, particularly the O-H/N-H stretch at approximately 3400 cm−1 and the C=O/C=C vibration at approximately 1600 cm−1, provide compelling qualitative evidence for successful biogenic synthesis of the nanoparticles.

This molecular-level capping mechanism directly dictates the crystalline and morphological architectures of the nanoparticles. XRD analysis (Fig. 3) confirmed the face-centered cubic (fcc) crystalline structure of metallic silver (JCPDS 04-0783) in all three species. However, the crystallite size calculated using the Scherrer equation for the (111) plane (Table S2, SI) varied significantly. *The H. psittacorum*-AgNPs exhibited the smallest crystallite size (20 ± 2 nm),

compared to 34 ± 3 nm for *E. cardamomum* and 41 ± 3 nm for *A. calcarata* AgNPs. This structural refinement directly correlates with the LC-MS/MS data; the smaller crystallite size of *H. psittacorum*-AgNPs is attributable to the steric hindrance imposed by the complex glycosides and protoalkaloids identified in Table 2, which effectively capped the silver nuclei and restricted further atomic addition (Fahim et al., 2024; Kaabipour & Hemmati, 2021).

Fig. 3 The X-ray Diffraction (XRD) patterns of silver nanoparticles (AgNPs) made from the leaf extracts of A. calcarata (red), E. cardamomum (green), and H. psittacorum (blue) are shown. All patterns confirmed the face-

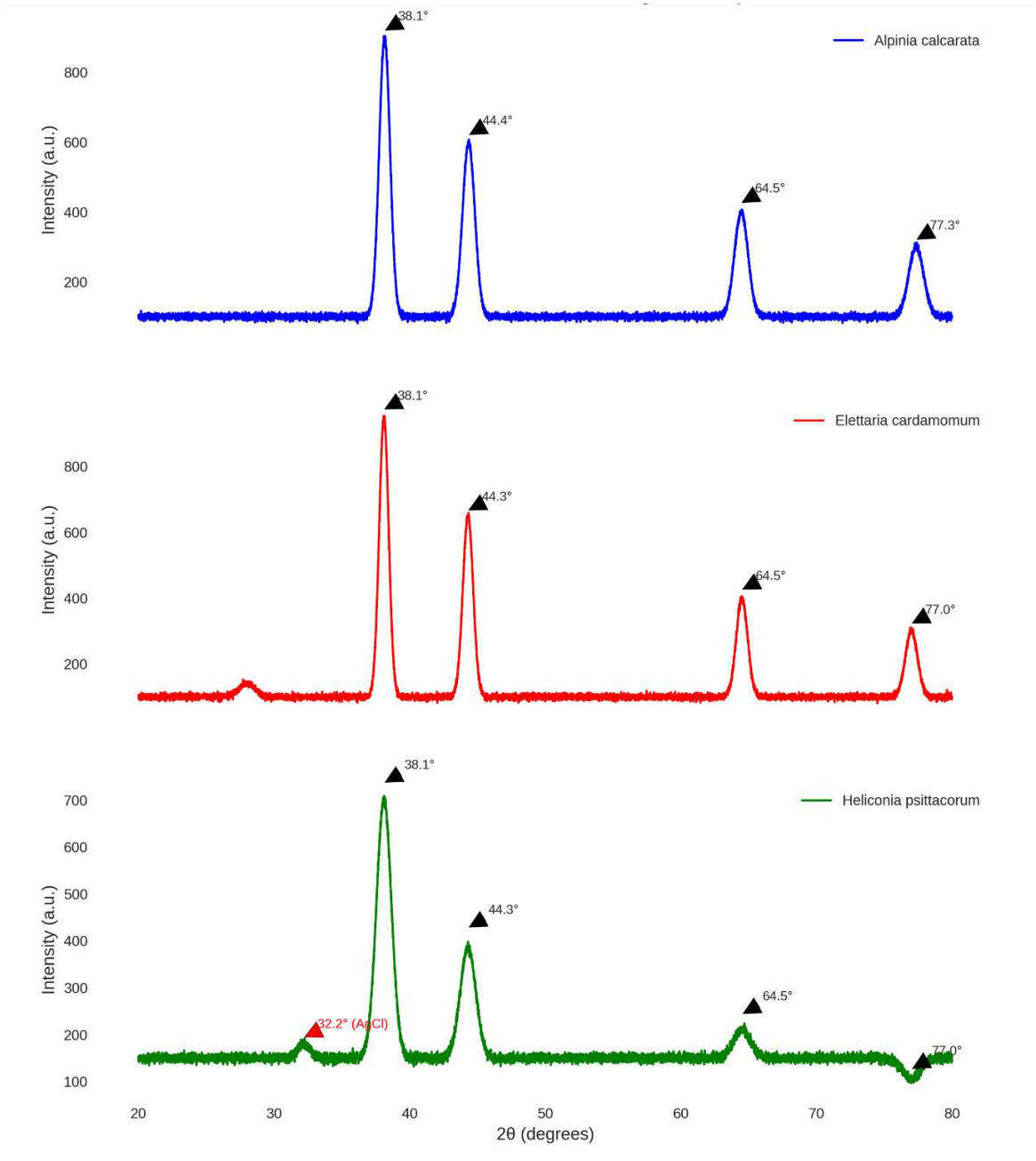

centered cubic (FCC) structure of metallic silver (Ag^0) with peaks at 38.1°, 44.3°, 64.5°, and 77.0°. No AgCl peaks were observed, and a broad peak at approximately 20 ° indicated the purity of silver and the successful organic coating.

This crystalline restriction translated into distinct morphological and colloidal properties. The SEM micrographs (Fig. 4) demonstrate that all formulations yielded predominantly spherical nanoparticles. While *H. psittacorum-AgNPs* exhibited a dominant population centered at ~20.3 nm, detailed ImageJ analysis revealed a secondary population of smaller nanoparticles (~10 nm), resulting in a bimodal size distribution that was more refined than the broader polydispersity observed for the other two extracts. EDX spectroscopy (Fig. 5) confirmed the high elemental purity of the Ag cores across all samples, with minor residual carbon and oxygen signals, exclusively attributable to the organic phytochemical corona (Vanlalveni et al., 2021). Furthermore, DLS analysis (Fig. 6) revealed that the hydrodynamic diameters were only marginally larger than the SEM core sizes (e.g., 27.2 nm for *H. psittacorum*), with low polydispersity indices (PDI < 0.3). This minimal disparity between the core and hydrodynamic size confirms that the phytochemical capping layer identified via LC-MS/MS is thin, uniform, and highly effective at preventing aqueous aggregation, as further supported by the strongly negative zeta potential values (<-20 mV) (Bhattacharjee, 2016; Danaei et al., 2018).

The apparent discrepancy between the crystallite size (XRD) and particle size (SEM) for *A. calcarata* and *E. cardamomum* arises from the polycrystalline nature of the larger secondary particles observed in the SEM images, where individual SEM-resolved particles are composed of multiple smaller crystalline domains that are tightly aggregated. The XRD-derived crystallite size reflects these individual coherent scattering domains, whereas SEM measures the overall aggregate diameter (Souza et al., 2016).

In contrast, *H. psittacorum*-AgNPs exhibited a more consistent crystalline structure. HR-TEM lattice fringe imaging confirmed the single-crystalline nature of the primary H. psittacorum-AgNP population (d-spacing consistent with the Ag fcc [111] plane), while a secondary population of larger particles was also observed (Fig. 4). Crucially, continuous lattice fringes were observed in both populations without distinct grain boundaries, confirming that the larger particles were single-crystalline domains resulting from accelerated growth rather than polycrystalline aggregates. This structural integrity is attributable to the superior capping efficiency of the alkaloid-rich corona, as identified by LC–MS/MS (Table 2).

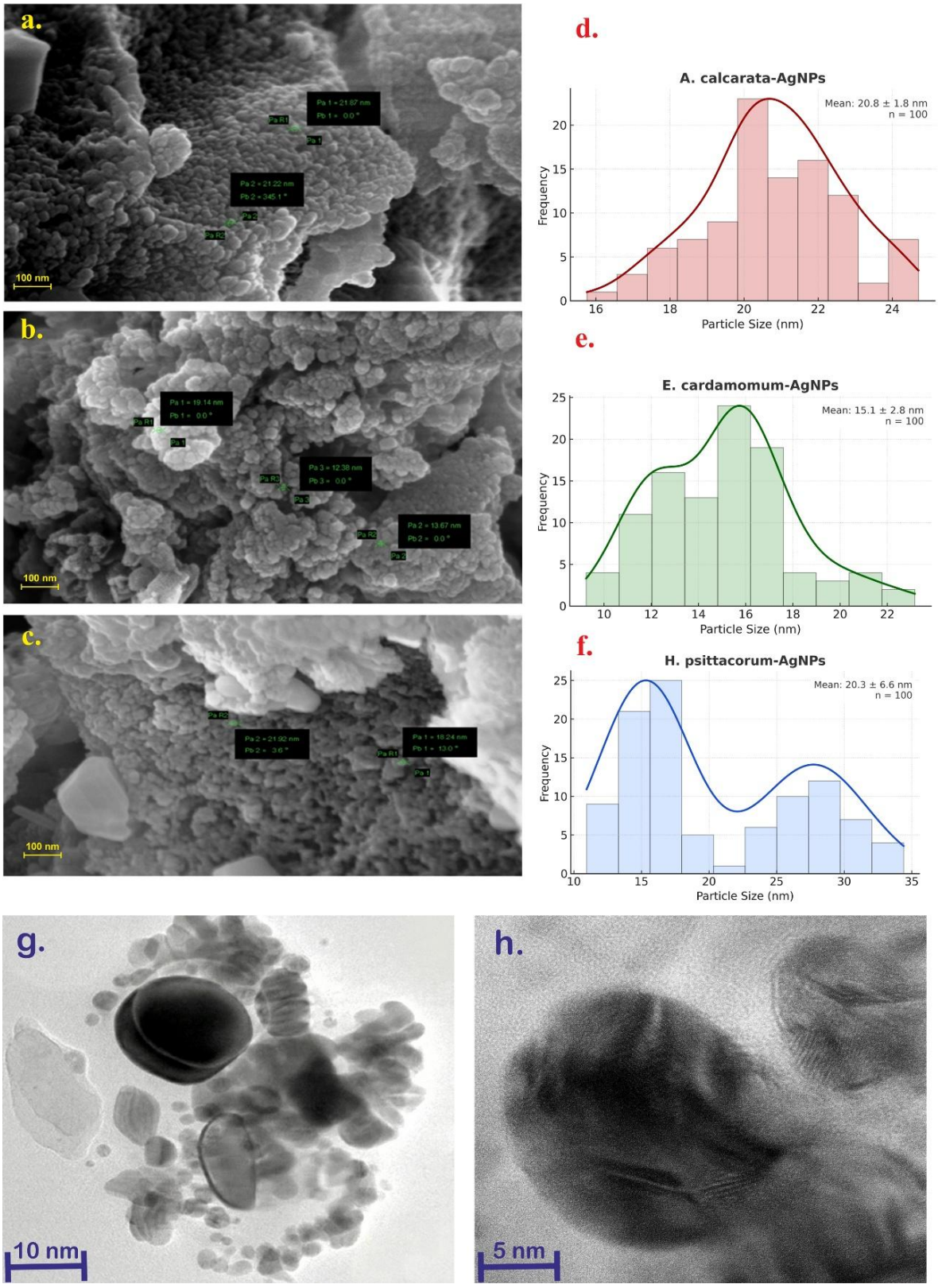

Fig. 4 The shape and size of the silver nanoparticles (AgNPs) produced by plants were studied. Scanning electron micrographs (SEM) showed that AgNPs made with (a) A. calcarata, (b) E. cardamomum, and (c) H. psittacorum were mainly round, with a scale of 100 nm. Size distribution charts generated using ImageJ (n > 100) indicated a bimodal population for H. psittacorum-AgNPs, with a dominant mode at ~20 nm and a secondary mode of smaller particles (~10 nm), resulting in an overall mean core diameter of 20.3 nm. High-resolution transmission electron microscopy (HR-TEM) of H. psittacorum-AgNPs revealed distinct lattice fringes (scale = 5 nm), confirming the single-crystalline nature of both the primary small particles (~10 nm) and larger aggregates.

Table 2. Major phytochemical compounds tentatively identified in the aqueous leaf extract of *Heliconia psittacorum* by LC–MS/MS and their proposed roles in the green synthesis and stabilization of AgNPs.

No.	Retention Time (min)	Observed m/z (ESI^+ / ESI^-)	Proposed Compound	Molecular Formula	Proposed Role in AgNP Formation and Stability
1	7.2	303 $[M+H]^+$ / 301 $[M-H]^-$	Phenolic compound (putative; possibly hydroxycinnamic acid derivative)	Not assigned	Primary reducing agent; contributes to the initial Ag^+ reduction due to high polarity and redox activity
2	11.1	465 $[M+H]^+$ / 463 $[M-H]^-$	Quercetin-3-O-glucoside	$C_{21}H_{20}O_{12}$	Steric stabilization enhances colloidal stability via hydrophilic glycosidic moieties.
3	14.9	287 $[M+H]^+$ / 285 $[M-H]^-$	Kaempferol	$C_{15}H_{10}O_6$	Secondary reducing agent; antioxidant support and surface interaction
4	15.2	360 $[M+H]^+$	Putative protoalkaloid (N-containing)	Not assigned	Surface capping agent; potential pH-responsive interaction with nanoparticle interface
5	21.4	500 $[M+H]^+$ / $[M-H]^-$	Terpenoid glycoside (putative)	Not assigned	Secondary stabilization contributes to the integrity and antioxidant capacity of the corona.

Notes:

1. Compounds were tentatively identified based on retention time (RT), accurate mass, and MS/MS fragmentation patterns using spectral databases (METLIN, NIST, and PubChem) with a similarity threshold of >80%.
2. The compound detected at 7.2 min (m/z 303/301) was initially assigned to quercetin based on mass; however, its early elution under reverse-phase conditions (C18 column) was inconsistent with the expected behavior of flavonol aglycones. Therefore, it was conservatively assigned as a polar phenolic compound (putative) pending further structural confirmation.
3. Under reverse-phase chromatographic conditions, glycosylated flavonoids elute earlier than their corresponding aglycones because of their increased polarity. The observed retention of quercetin-3-O-glucoside (11.1 min) relative to kaempferol (14.9 min) is consistent with this observation.
4. The compounds listed in entries 3 and 4 eluted within a narrow retention window (14.9 min and 15.2 min, respectively) but were unambiguously distinguished by distinct MS/MS fragmentation patterns: (i) kaempferol was identified by characteristic retro-Diels-Alder (RDA) cleavage product ions at m/z 153 and 121 (match score: METLIN >85%); (ii) the protoalkaloid was detected with a nitrogen-containing fragment at m/z 136 in positive mode, which was absent in flavonoid spectra (match score: NIST >82%). These two compounds were confirmed to be distinct chemical entities.
5. Molecular formulas were not assigned to the putative compounds (entries 1, 4, and 5) because of the absence of high-resolution mass spectrometry (HRMS) data and authentic reference standards. Consequently, identifications were reported at Level 2 (putative annotation) in accordance with the Metabolomics Standards Initiative (MSI) guidelines.
6. The proposed functional roles in AgNP synthesis are inferred from known chemical reactivity patterns (e.g., hydroxyl-mediated reduction and nitrogen-based coordination). These findings should be interpreted as correlative rather than mechanistically confirmed.

Furthermore, the distinct metabolomic profile of *H. psittacorum*, characterized by a high abundance of glycosylated flavonoids (e.g., Quercetin-3-O-glucoside) and nitrogenous protoalkaloids, provides dual stabilization mechanisms. Colloidal stability assays in deionized water confirmed nanoparticle integrity under baseline conditions (Table S1, SI), and the presence of these hydrophilic glycosides offered robust steric stabilization in complex biological media. This mechanism effectively prevents protein corona-induced aggregation in

DMEM cell culture media by forming a resilient physical barrier, thereby ensuring consistent dispersion and reliability during bioassays(Nargis et al., 2019; Xiao & Högger, 2015; Zhou et

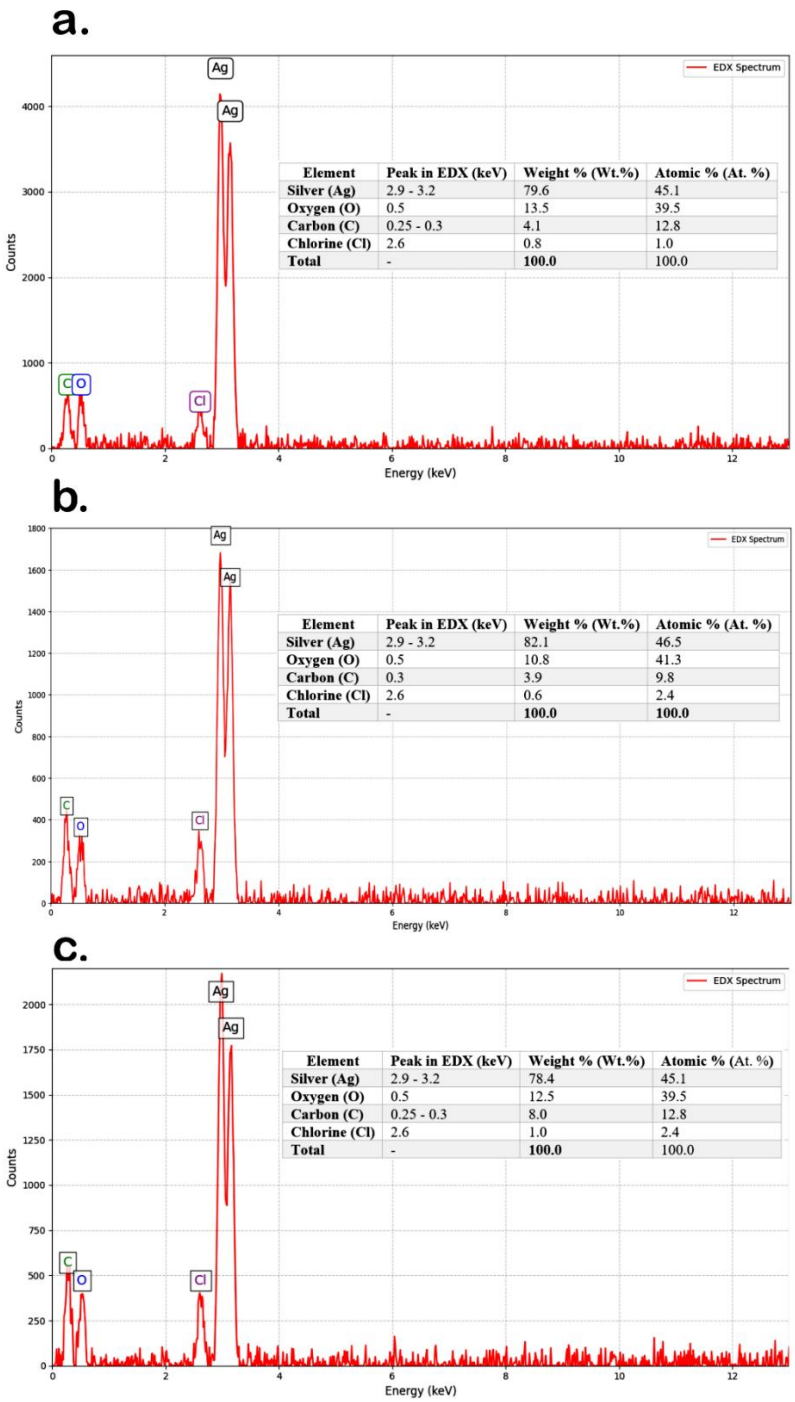

al., 2023).

Fig. 5 Energy-dispersive X-ray (EDX) spectroscopy was used to check the elements in silver nanoparticles (AgNPs) made from three Zingiberales plant extracts: (a) Alpinia calcarata AgNPs, (b) Elettaria cardamomum AgNPs, and (c) Heliconia psittacorum AgNPs. Peaks at 2.9–3.2 keV indicate the presence of metallic silver (Ag). The analysis showed a high silver content (79.6–82.1 wt%), confirming that the AgNPs were well prepared and pure. Small peaks for carbon (C), oxygen (O), and chlorine (Cl) were due to organic capping agents derived from plant chemicals such as phenolics, flavonoids, and alkaloids, which is consistent with the FTIR results (Fig.2).

The small amount of chlorine (Cl) likely originated from residual chloride ions in the plant extract that remained on the nanoparticle surface after washing.

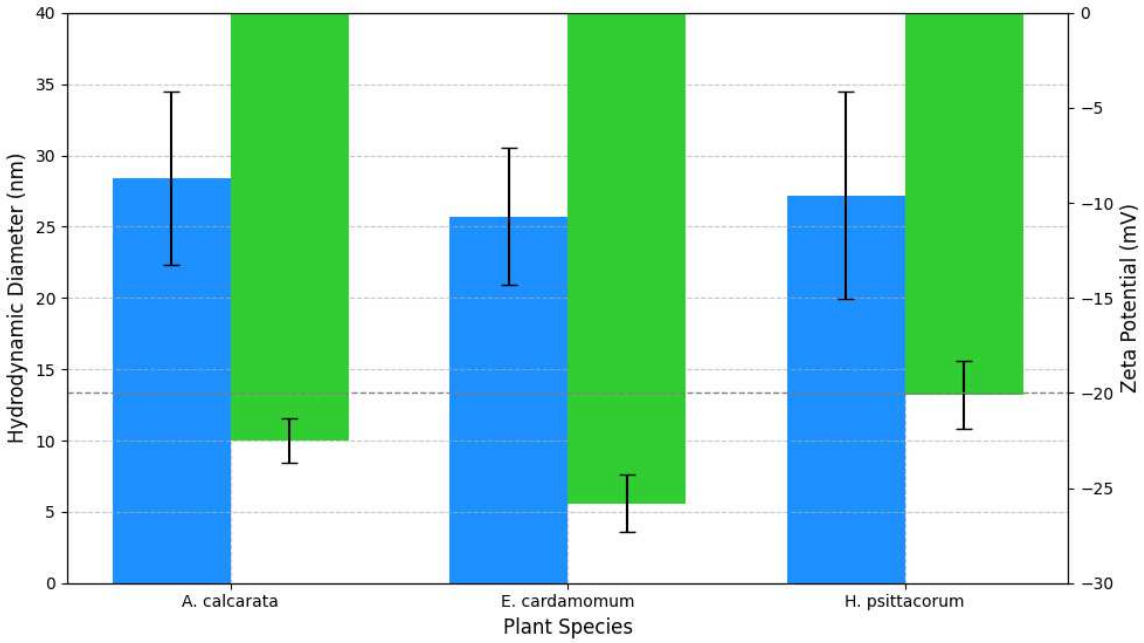

Fig. 6 Comparison of the hydrodynamic size and surface charge of the synthesized AgNPs. Interestingly, while *H. Psittacorum* exhibited the smallest crystalline/core size (via XRD/SEM). DLS analysis revealed that E. cardamomum formed the smallest hydrodynamic complexes (25.7 nm), likely due to differences in the hydration of the capping layer. All nanoparticles possessed a strongly negative charge ($|\zeta| \geq 20$ mV), indicating high colloidal stability driven by plant-derived phytochemicals.

3.3. Stimuli-Responsive Ag^+ Release Kinetics

Beyond structural stabilization, the phytochemical corona identified in Section 3.2 plays a critical role in determining the dissolution kinetics of AgNPs in biological microenvironments. To evaluate whether the biogenic capping layer imparts stimuli-responsive behavior, the *in vitro* release profile of Ag^+ ions from *H. psittacorum*-AgNPs was monitored over 72 h at physiological pH (7.4) and tumor-mimetic acidic pH (5.5) using a dialysis bag diffusion method (Fig. 7). The cumulative release profiles exhibited a distinct biphasic pattern: an initial burst release within the first 8 h, followed by a sustained release phase (Bélteky et al., 2019). As quantified in Table 3, the release kinetics were highly dependent on pH. At physiological pH (7.4), the cumulative release reached only 47.8% after 72 h, with a relatively subdued burst release of 16.9% in the first 8 h. In stark contrast, exposure to an acidic tumor-mimetic environment (pH 5.5) triggered substantially accelerated dissolution, resulting in 81.0% cumulative release and 40.0% burst release within the same 8-hour window. The pronounced pH-responsiveness can be mechanistically traced back to the LC-MS/MS results (Table 2). This pronounced pH responsiveness can be mechanistically attributed to the LC-MS findings (Table 2), in which protonation of nitrogenous groups within the protoalkaloids and acid-

catalyzed hydrolysis of glycosidic bonds in the capping layer at pH 5.5 weaken the ligand-talcoordination. The pH-triggered release is attributed to the protonation of nitrogenous protoalkaloids in the biogenic corona at an acidic pH, which reduces the electrostatic attraction between the capping layer and the AgNP surface, thereby facilitating ion diffusion. This structural loosening of the phytochemical corona facilitates rapid Ag^+ diffusion out of the nanoparticle matrix, whereas the intact corona at pH 7.4 effectively retains the silver core (Raza et al., 2023; Singh et al., 2016).

Table 3. Kinetic parameters and Cumulative Release of Ag^+ from H. psittacorum-AgNPs at different pH values (mean ± SD, n = 3).

Release Model	Parameter	pH 7.4 (Physiological)	pH 5.5 (Tumor-mimetic)
Korsmeyer-Peppas	R^2	> 0.95	> 0.97
	n (exponent)	0.43	0.69
	K (constant)	0.021	0.048
Cumulative Release	At 8 h (%)	16.9 ± 1.2	40.0 ± 2.7
	At 72 h (%)	47.8 ± 3.2	81.0 ± 4.9

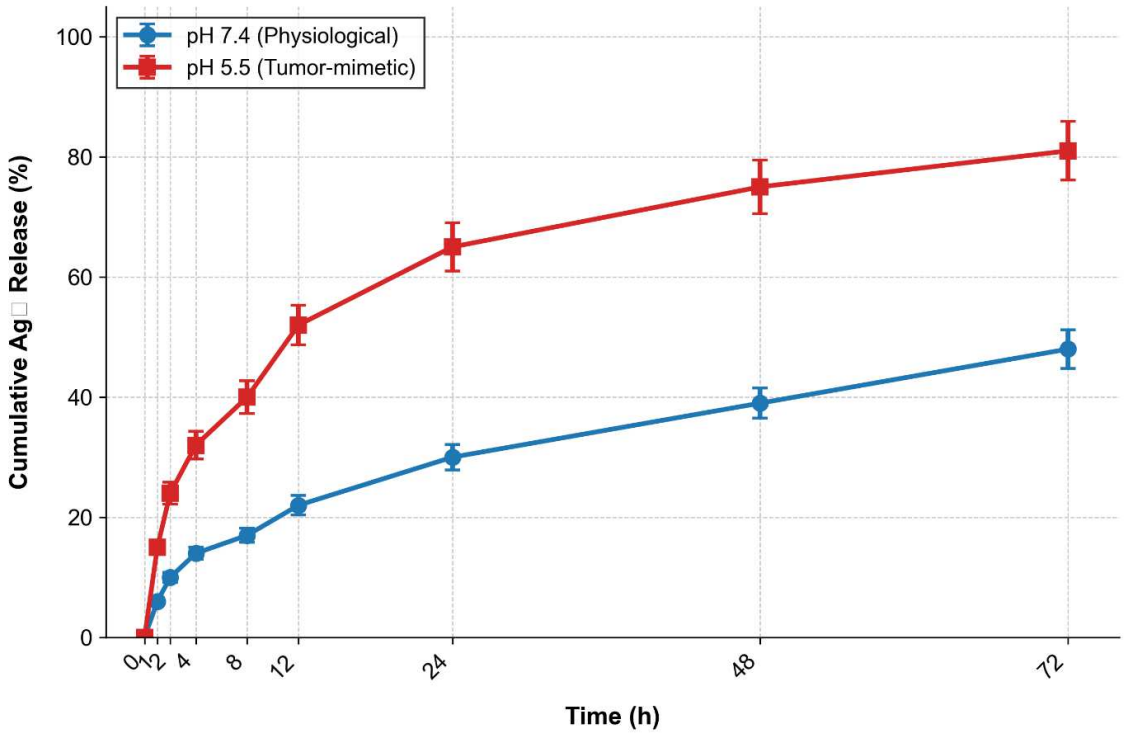

Fig. 7. In vitro cumulative Ag^+ release profiles of *H. psittacorum*-AgNPs under physiological (pH 7.4) and tumor-mimetic acidic (pH 5.5) conditions over 72 h. Data points represent the mean ± standard deviation (SD, n = 3 independent replicates). Both profiles exhibited a biphasic release pattern, characterized by an initial burst release within the first 8 h, followed by a sustained release phase. Notably, the cumulative ion release at pH 5.5 (81.0%) was significantly accelerated compared to that at pH 7.4 (47.8%). This pronounced pH-responsive behavior is attributed to the acid-catalyzed protonation of nitrogenous protoalkaloids and hydrolysis of glycosidic bonds

within the phytochemical corona, compromising its structural integrity and facilitating the rapid diffusion of Ag^+ ions in the acidic tumor microenvironment.

To mathematically elucidate this release mechanism, the data were fitted to the kinetic models. The release profiles at both pH levels demonstrated the best fit to Korsmeyer–Peppas model ($R^2 > 0.95$). The release exponent (n) provided critical insight into the transport phenomena: an n value of 0.43 at pH 7.4 indicates a classical Fickian diffusion mechanism. Conversely, the n value increased to 0.69 at pH 5.5, signifying an anomalous (non-Fickian) transport mechanism. This shift confirms that under acidic conditions, Ag^+release is governed by a synergistic combination of diffusion and the physical erosion/swelling of the phytochemical corona (Taherpour et al., 2025). These parameters were validated against a standard calibration curve (Fig. S1, SI), demonstrating that the green-synthesized *H. psittacorum*-AgNPs function as smart material intermediates that preferentially release their active metallic payloads in the acidic tumor microenvironment.

3.4. Comparative Analysis with State-of-the-Art Green Synthesis

To contextualize the novelty of the present green synthesis framework, a comparative analysis was conducted with recent high-impact studies utilizing plant extracts from the order Zingiberales and related medicinal species (Table 4). While previous studies have successfully demonstrated the bioreduction capabilities of these plants, most rely on conventional endpoint characterizations without establishing a molecular-level structure–activity relationship (SAR) or evaluating the stimuli-responsive behavior (Ilavenil et al., 2025).

Table 4. Comparative analysis of the green synthesis of AgNPs using Zingiberales and related medicinal-plant extracts.

Plant Species (Family)	Temp (°C) / Time	Precursor Conc.	Size (nm) [Method]	IC_{50} (MCF-7)	Phytochemical Profiling	Key Mechanistic Feature / Advantage
Heliconia psittacorum **(Heliconiaceae) (This study)**	60 °C / 60 min	0.1 mM	20.3 [SEM]	32.8 µg/mL	LC-MS/MS (Targeted metabolites)	LC-MS-guided SAR; pH-responsive Ag^+ release (Korsmeyer-Peppas modeling)
Alpinia calcarata **(Zingiberaceae) (Pugazhendhi et al., 2015)**	75 °C / 24 h	0.2 mM	5–15 [HRTEM]	Not evaluated	Qualitative FTIR	Basic characterization; no biological evaluation against cancer cells.
Elettaria cardamomum **(Zingiberaceae) (Al-Saleh et al., 2025)**	~100 °C (Boiling) / 30 min	1.77–8.83 mM	24.5 [TEM]	Not evaluated (Genotoxicity focus)	GC-MS (Essential oil profile)	High precursor concentration; focused on genotoxicity, not smart release.

***Zingiber officinale* (Zingiberaceae) (Ongtanasup et al., 2024)**	RT / 30 min	2.0 mM	32.6 [DLS]	Not evaluated	Qualitative Colorimetric	High precursor concentration; lack of targeted metabolomic identification.
***Astragalus fasciculifolius* (Fabaceae) (Nosrati et al., 2025)**	RT / 300 min	1–5 mM	16 [TEM]	21.7 µg/mL	Qualitative Colorimetric	Extremely long synthesis time and no pH-responsive release kinetics.
***Magnolia alba* (Magnoliaceae) (De Mel et al., 2025)**	95 °C / 30 min	10 mM	40 [SEM]	20–40% inhibition*	Qualitative Phytochemical	Very high energy/precursor input; lacked LC-MS or release kinetics.

**Inhibition percentage reported at a single high concentration, not calculated IC_{50} via nonlinear regression.*

As shown in Table 4, this study offers distinct advantages. First, the synthetic protocol operates at a moderate temperature (60 °C) and low precursor concentration (0.1 mM), representing a lower energy footprint than protocols requiring elevated temperatures (e.g., 95 °C for *Magnolia alba*;(De Mel et al., 2025)) or boiling conditions (e.g., *Elettaria cardamomum*,(Al-Saleh et al., 2025)).

Second, *H. psittacorum*-AgNPs exhibited a competitive IC_{50} value of 32.8 µg/mL for MCF-7 cells. This value is slightly higher than the 21.7 µg/mL reported for *Astragalus fasciculifolius* (Nosrati et al., 2025), but protocol differences limit a direct numerical comparison. Notably, Nosrati et al. reported their IC_{50} after a shorter 24 h exposure, whereas our value was determined using a standardized 48 h incubation period and rigorously corrected for optical interference. Despite the longer incubation time, which typically necessitates higher concentrations to induce cytotoxicity, our formulation maintained competitive potency. More importantly, our study uniquely provides a quantitative selectivity index (SI ≥ 6.1) and pH-responsive release kinetics—critical therapeutic parameters not evaluated in the aforementioned study—and is significantly more potent than the qualitative inhibition observed in other Zingiberales studies (Ongtanasup et al., 2024).

Finally, unlike the studies listed in Table 4, which rely on qualitative phytochemical screening, the integration of LC–MS/MS metabolomic fingerprinting in this study precisely identified the capping ligands. This molecular-level resolution directly explains the superior control over the crystallite size and enables a rational interpretation of the pH-responsive Ag^+ release kinetics (81% at pH 5.5 vs. 48% at pH 7.4). Therefore, this study transcends conventional empirical green synthesis by providing a fully characterized, eco-friendly, and intelligent nanomaterial platform (Sebaugh, 2011).

3.5. Biomedical Efficacy and Mechanistic Validation

To validate that the optimized, phytochemically tuned AgNPs exhibited functional bioactivity beyond their structural characterization, their antibacterial and anticancer efficacies were assessed. Antibacterial potency was assessed against clinically relevant pathogens, including MRSA and Gram-negative strains (Table 5). All biogenic AgNPs exhibited concentration-dependent bactericidal activity, with *H. psittacorum*-AgNPs demonstrating the highest efficacy (MIC range: 6.25–12.5 µg/mL). Specifically, the lower limit of this range (6.25 µg/mL against MRSA and *E. coli*) represents a significant improvement in potency compared to formulations derived from *A. calcarata* and *E. cardamomum* (Table 5). Reporting results as ranges for the latter two accounts for the inherent resolution limit of the 2-fold serial dilution method, providing a robust representation of bactericidal efficacy within the limits of the assay protocol (Wiegand et al., 2008). The preliminary agar well diffusion assay corroborated these findings in a concentration-dependent manner for all three formulations (Table S5; Fig. S2, S3, and S4, SI). *H. psittacorum*-AgNPs exhibited the largest inhibition zones against the majority of tested pathogens (MRSA, *K. pneumoniae*, and *P. aeruginosa*), with the notable exception of *E. coli*, against which *A. calcarata*-AgNPs produced marginally larger zones in the agar diffusion assay (Table S5, SI). This discrepancy is attributed to differences in nanoparticle diffusion kinetics in solid agar, as broth microdilution-based MIC values (Table 5), which are independent of diffusion, consistently confirm the superior potency of *H. psittacorum*-AgNPs. An MBC/MIC ratio of 2.0 confirms a bactericidal rather than a bacteriostatic mechanism, indicating complete microbial eradication(Pankey & Sabath, 2004). This superior profile directly correlates with the smaller crystallite size and high surface area-to-volume ratio identified in Section 3.2, which facilitates enhanced physical interactions with bacterial cell walls (More et al., 2023; Vanlalveni et al., 2021).

Table 5. Minimum Inhibitory Concentration (MIC) and Minimum Bactericidal Concentration (MBC) Values (µg/mL, Mean ± SD, n = 3) for AgNPs Against Pathogens

Formulation	Pathogen	MIC (µg/mL)	MBC (µg/mL)	MBC/MIC Ratio
A. calcarata–AgNPs	MRSA / E. coli / K. p. / P. a.	25–50†	50 – 100†	2.0
E. cardamomum–AgNPs	MRSA / E. coli / K. p. / P. a.	12.5–25†	25 – 50†	2.0
H. psittacorum–AgNPs	MRSA / E. coli	6.25 ± 1.1	12.5 ± 1.4	2.0
	K. p. / P. a.	12.5 ± 1.3	25 ± 1.6	2.0
Crude Extracts	All Strains	>200	>200	–
$AgNO_3$ (0.1 mM)	All Strains	>100	>200	–

Gentamicin	All Strains	4 – 8	8 – 16	2.0

Note: † MIC and MBC values for *A. calcarata* and *E. cardamomum* are expressed as ranges reflecting the inherent resolution limit of the 2-fold serial dilution method (CLSI M07, 2020), in which true endpoint detection varies by ±1 dilution step between replicates. For *H. psittacorum*-AgNPs, the SD values reflected the variability in endpoint detection across three independent biological replicates.

Anticancer cytotoxicity was evaluated against MCF-7 breast adenocarcinoma cells, with non-cancerous HEK-293 cells serving as a biocompatibility control (Table 6; Fig. 8). H. psittacorum-AgNPs exhibited an IC_{50} of 32.8 ± 2.4 µg/mL and a favorable selectivity index (SI ≥ 6.1), indicating preferential toxicity toward malignant cells. Notably, MTT optical interference controls confirmed that the observed cytotoxicity was strictly biological and not an artifact of the nanoparticle-dye interaction (Murphy et al., 2022).

Table 6. Cytotoxicity of biogenic AgNPs against MCF-7 and HEK-293 cells after 48 h of exposure. IC_{50} values were determined using the MTT assay and corrected for optical interference using cell-free controls (Table S6 and Fig. S5, SI). The selectivity index (SI) was calculated as IC_{50}(HEK-293)/IC_{50}(MCF-7); the IC_{50} for HEK-293 cells was not reached at concentrations of up to 200 µg/mL.

Formulation	Cell Line	IC_{50} (µg/mL)	95% CI	SI
A. calcarata–AgNPs	MCF-7	110.5 ± 8.2	95 – 125	> 1.8
	HEK-293	> 200	N/A	–
E. cardamomum–AgNPs	MCF-7	85.2 ± 6.4	72 – 98	> 2.3
	HEK-293	> 200	N/A	–
H. psittacorum-AgNPs	MCF-7	32.8 ± 2.4	28.1 – 38.3	≥ 6.1
	HEK-293	> 200	N/A	–
Camptothecin	MCF-7	1.8 ± 0.1	1.5 – 2.1	–

Note: SI > 2 is generally considered indicative of good selectivity. Values are reported as lower-bound estimates (> or ≥) based on an upper IC_{50} limit of 200 µg/mL for HEK-293 cells.

Mechanistically, intracellular ROS generation (Fig. 9) and JC-1 mitochondrial depolarization (Fig. 10) revealed significant oxidative stress and mitochondrial dysfunction in the treated MCF-7 cells. (Gooz & Maldonado, 2023; Gurunathan et al., 2012). These mechanistic indicators provide functional validation of the in vitro pH-responsive dissolution model established in Section 3.3. The observed cellular stress directly correlated with the preferential release of toxic Ag^+ ions in the acidic tumor microenvironment, confirming that the smart phytochemical corona drives biomedical efficacy(Raza et al., 2023; Taherpour et al., 2025).

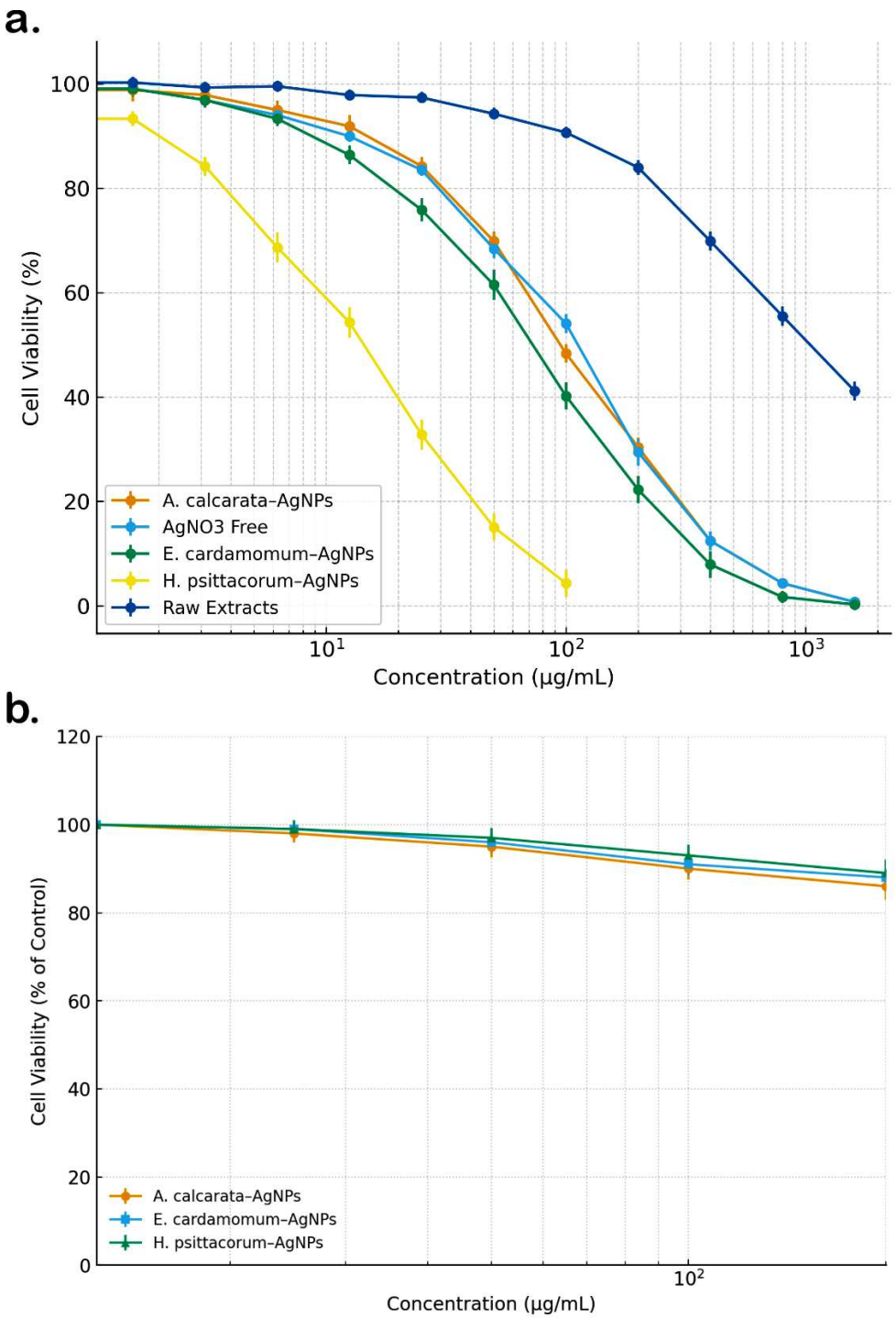

Fig. 8 Cytotoxicity profiles of biogenic AgNPs against (a) MCF-7 breast cancer cells and (b) non-cancerous HEK-293 cells after 48 h of exposure. Cells were treated with AgNPs derived from *A. calcarata*, *E. cardamomum*, and *H. psittacorum* at concentrations ranging from 12.5 to 200 µg mL^{-1}, alongside crude plant extracts, $AgNO_3$, and camptothecin (positive control). Data are presented as mean ± SD of three independent biological replicates (each with three technical replicates), normalized to the untreated controls. For MCF-7 cells, dose-dependent cytotoxicity was observed across all AgNP formulations, with *H. psittacorum*-AgNPs exhibiting the steepest decline in viability of the cells. For HEK-293 cells, all biogenic AgNPs demonstrated significantly reduced cytotoxicity, with IC_{50} values exceeding 200 µg mL^{-1}, indicating favorable biocompatibility of the AgNPs. The statistical significance of the IC_{50} differences was determined using one-way ANOVA ($F_{2,6} = 45.2$, $p < 0.0001$), followed by Tukey's post hoc test ($p < 0.05$). The corresponding selectivity indices (SI) are summarized in Table 6.

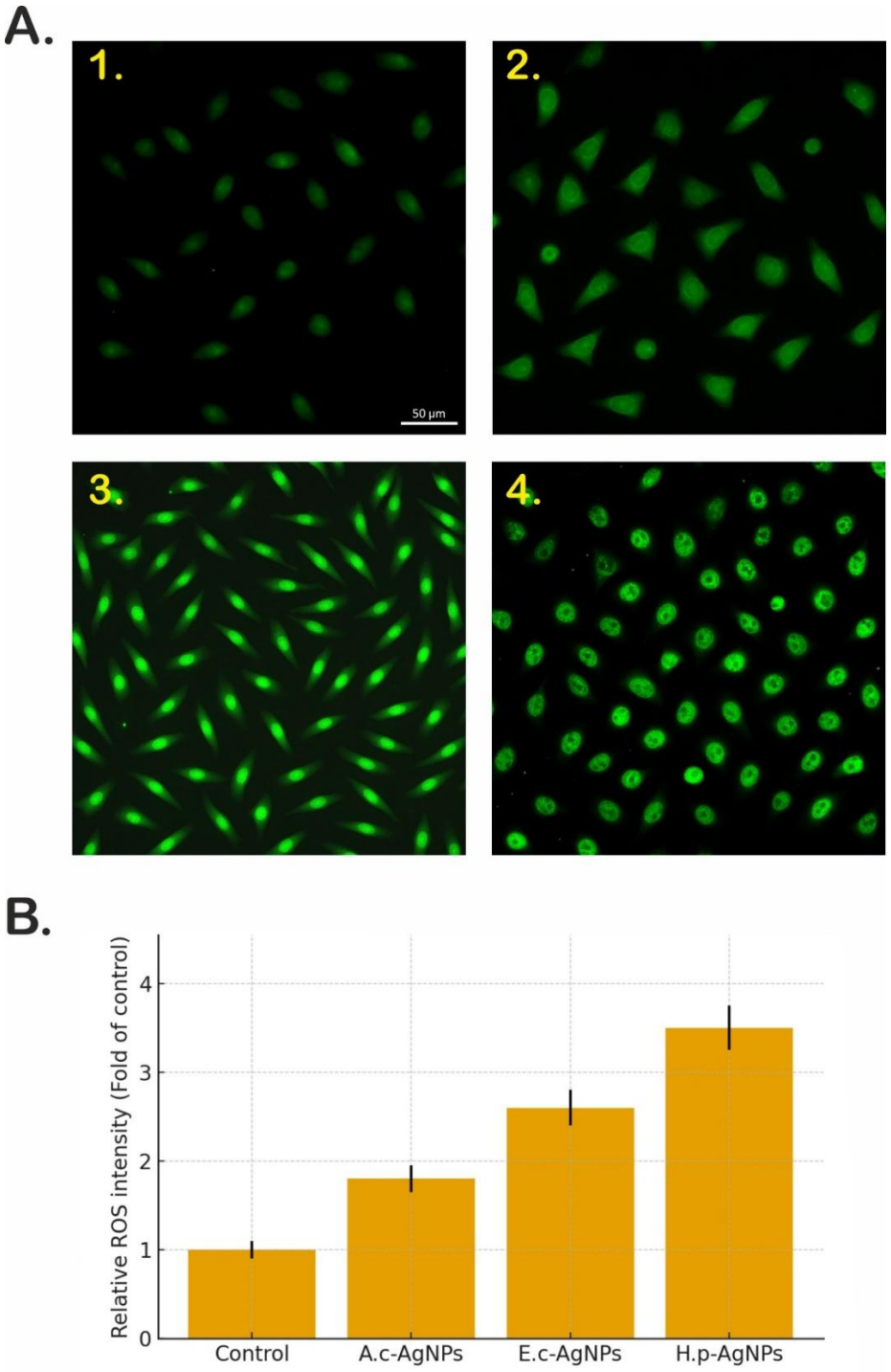

Fig. 9. Intracellular reactive oxygen species (ROS) generation in MCF-7 breast cancer cells after 24 h of exposure to biogenic AgNPs. (A) Representative fluorescence micrographs of dichlorofluorescein diacetate (DCFH-DA)-stained cells. (1) Untreated control cells exhibited negligible background fluorescence, indicating basal ROS levels. (2) Cells treated with *A. calcarata*–AgNPs (IC_{50} = 110.5 µg/mL) exhibited a moderate increase in green fluorescence. (3) Treatment with *E. cardamomum*–AgNPs (IC_{50} = 85.2 µg/mL) markedly enhanced fluorescence intensity. (4) Exposure to *H. psittacorum*–AgNPs (IC_{50} = 32.8 µg/mL) induced the most pronounced fluorescence, accompanied by morphological changes consistent with oxidative stress. Scale bar = 50 µm. (B) Quantitative analysis of the mean fluorescence intensity (MFI) normalized to the untreated controls. Data are presented as mean ± SD (n = 3 independent biological replicates). Statistical significance was determined using one-way ANOVA followed by Tukey's post-hoc test ($p < 0.001$ vs. control). The relative ROS induction followed the trend *H. psittacorum* > *E. cardamomum* > *A. calcarata*, which was inversely correlated with their respective IC_{50} values (Table 6). Fluorescence intensity was quantified using the ImageJ software.

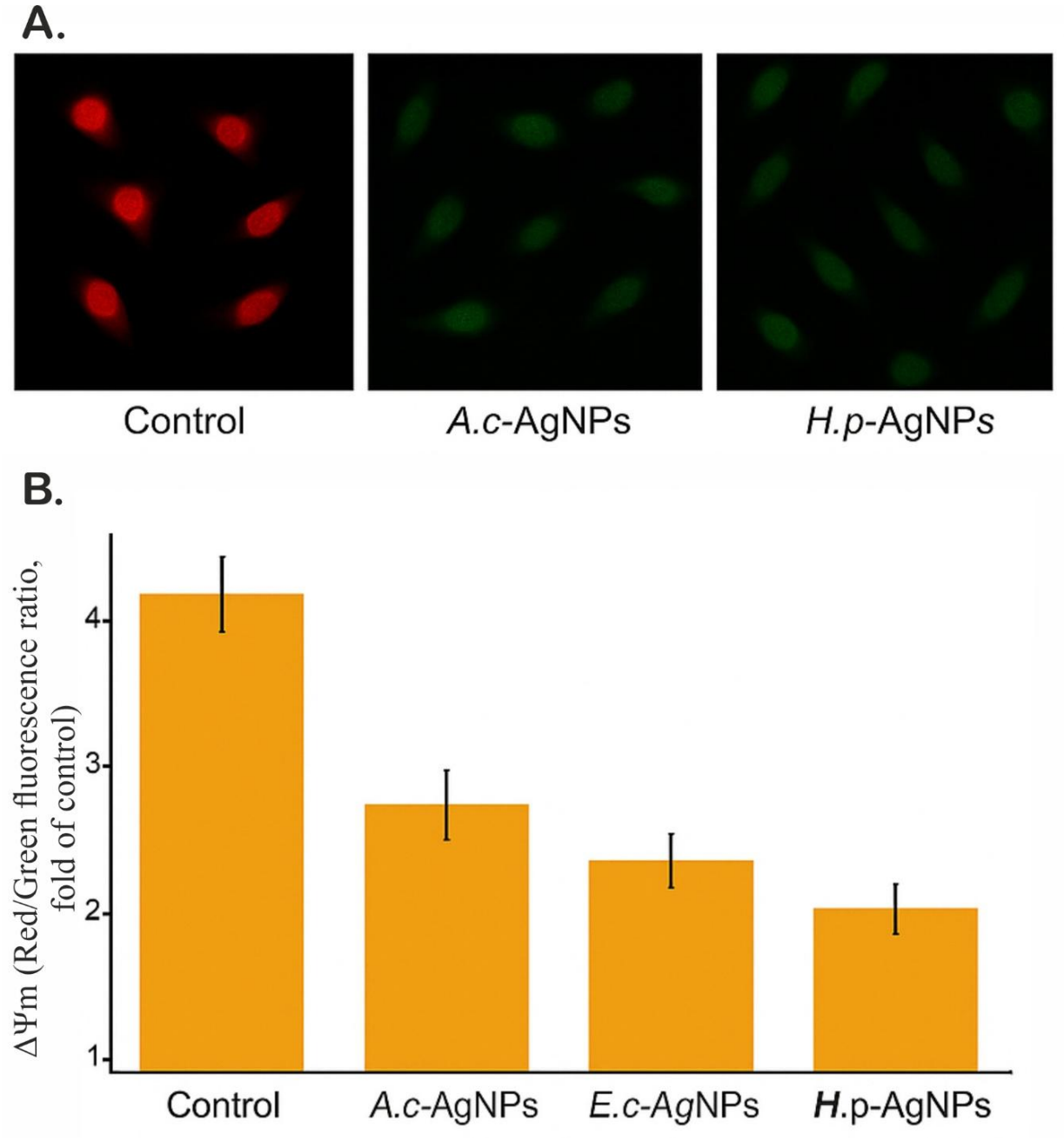

Fig. 10. Assessment of mitochondrial membrane potential (ΔΨm) dissipation in MCF-7 breast cancer cells following 24 h exposure to biogenic AgNPs using JC-1 ratiometric staining. (A) Representative merged fluorescence micrographs showing JC-1 aggregates (red fluorescence; intact/healthy mitochondria) and JC-1 monomers (green fluorescence; depolarized/dysfunctional mitochondria). Untreated control cells predominantly exhibited red fluorescence, indicating a preserved ΔΨm. Treatment with *A. calcarata*–AgNPs and *E. cardamomum*–AgNPs resulted in a moderate increase in green fluorescence, whereas exposure to *H. psittacorum*–AgNPs induced a pronounced shift toward green fluorescence, indicating extensive mitochondrial depolarization. Scale bar = 50 µm. (B) Quantitative analysis of the red-to-green fluorescence intensity ratio. Data are presented as mean ± SD (n = 3 independent biological replicates). Statistical significance was determined by one-way ANOVA followed by Tukey's post hoc test ($p < 0.001$ *vs. control). The progressive loss of ΔΨm across the three formulations (*H. psittacorum* > *E. cardamomum* > *A. calcarata*) correlated inversely with their respective IC_{50} values (Table 6) and directly with the observed increase in intracellular ROS levels (Fig. 9). Fluorescence intensity was quantified using the ImageJ software.

3.6. Study Limitations

As a study fundamentally focused on advancing green synthesis methodologies and phytochemical–structure relationships, we prioritized metabolomic and physicochemical characterization over exhaustive molecular biology validation. While LC–MS/MS fingerprinting has identified the major capping ligands, determining the individual reduction kinetics of each isolated biomolecule remains a prospective objective (Fahim et al., 2024). Furthermore, although the stimuli-responsive Ag^{+} release and subsequent ROS generation strongly suggest a tumor-targeted mechanism, validating that the precise downstream apoptotic cascades (e.g., caspase activation) were beyond the scope of this investigation (Zubair & Bokhari, 2025). Future translational studies are required to fully elucidate the in vivo pharmacokinetics of Heliconiaceae-derived nanomaterials.

4. Conclusion

This study effectively illustrates that precise phytochemical mapping is crucial for understanding the structural and functional outcomes of plant-mediated green synthesis within the framework of sustainable pharmacy. By examining three species within the order *Zingiberales*, we determined that it is the extract's specific metabolomic composition, rather than just the reduction parameters, that dictates nanoparticle architecture. The integration of LC–MS/MS fingerprinting with conventional spectroscopic and electron microscopy techniques provided unambiguous evidence that nitrogenous protoalkaloids and flavonoid glycosides in *Heliconia psittacorum* exert a steric hindrance effect during nucleation, yielding nanoparticles with significantly refined crystallite sizes compared to terpenoid-rich *Zingiberaceae* extracts. Furthermore, the synthetic protocol was optimized to adhere strictly to green chemistry metrics, using a remarkably low precursor concentration (0.1 mM) and moderate thermal energy input (60°C), thereby minimizing the environmental footprint and demonstrating a highly efficient model for green pharmaceutical manufacturing compared to conventional high-temperature or high-concentration biogenic methods.

The primary mechanistic advancement of this work lies in the transition of green-synthesized AgNPs from passive colloidal systems to stimuli-responsive pharmaceutical platforms. By correlating the LC-MS/MS-derived corona chemistry with in vitro dissolution kinetics, we elucidated that the alkaloid-rich capping layer of *H. psittacorum*-AgNPs acts as a pH-sensitive gatekeeper. The distinct shift from Fickian diffusion at physiological pH to anomalous transport at tumor-mimetic acidic pH confirms that the biogenic corona facilitates preferential

Ag^+ release in pathological microenvironments. As contextualized by our comparative analysis (Table 4), this metabolomic-to-kinetic correlation represents a significant paradigm shift from the empirical screening approaches that currently dominate *Zingiberales*-derived nanotechnology, explaining both the superior size control and targeted biological efficacy without relying on synthetic polymeric coatings. Consequently, the *H. psittacorum*-AgNPs developed herein fulfill the dual criteria of sustainable nanomanufacturing and smart therapeutic potential, exhibiting potent, selective antibacterial and anticancer activities driven by ROS generation (as detailed in Tables 2 and 3). While the current biological assessments robustly validate the in vitro efficacy and the smart-release concept, definitive elucidation of the intracellular apoptotic cascades and in vivo pharmacokinetic profiles remains a prospective objective. Ultimately, this work establishes a reproducible, eco-friendly framework that leverages untargeted metabolomics to engineer intelligent phytochemical coronas, bridging the critical knowledge gap between botanical biodiversity and precision sustainable pharmaceutical design.

Declarations

Funding
The authors declare that no funds, grants, or other support were received during the preparation of this manuscript. This research did not receive any specific grants from funding agencies in the public, commercial, or not-for-profit sectors.

Competing Interests
The authors declare that they have no competing financial interests or personal relationships that could have influenced the work reported in this paper.

Ethics Approval
This study adhered to ethical guidelines for laboratory-based scientific research involving plant materials, microbial strains, and established human cell lines. Freshly collected leaves from Alpinia calcarata, Elettaria cardamomum, and Heliconia psittacorum were used with proper institutional authorization from the Botanical Garden of the University of Calicut (permit no. CUBG-2023-045). Standard bacterial strains (ATCC 27853, ATCC 43300, ATCC 25922, and ATCC 700603) and commercially available human cell lines (MCF-7, ATCC HTB-22, and HEK-293) were used. No experiments were performed on human participants, human tissues or live vertebrates.

Consent to Participate
Not applicable. This study did not involve any human participants.

Consent to Publish
Not applicable. This study did not include any personal data.

Author Contributions (CRediT)
Seyed Mohammad Faghih: Conceptualization, Methodology, Formal analysis, Investigation, Writing - original draft, Supervision.
Najim Obaid Dawood: Validation, Writing - review & editing.
Mazin Abdulhussein Beden: Methodology, Validation, Writing - review & editing.
All authors have read and approved the final manuscript.

Data Availability

All data generated or analyzed during this study are included in this published article and its supplementary information. Raw and processed datasets are available from the corresponding author upon reasonable request.

Declaration of Generative AI and AI-Assisted Technologies in the Writing Process
During the preparation of this manuscript, the authors used generative AI tools solely to improve the readability and grammatical accuracy of the English text. After using this service, the authors reviewed and edited the content as needed and took full responsibility for the scientific integrity and accuracy of the published article.

Reference:

Ahmed, S., Ahmad, M., Swami, B. L., & Ikram, S. (2016). A review on plants extract mediated synthesis of silver nanoparticles for antimicrobial applications: A green expertise. *Journal of Advanced Research*, *7*(1), 17–28. https://doi.org/10.1016/j.jare.2015.02.007

Al-Saleh, M. A., Al-Harbi, H. F., Al-Humaid, L., & Awad, M. A. (2025). An assessment of the Cyto-Genotoxicity Effects of Green-Synthesized Silver Nanoparticles and ATCBRA insecticide on the root system of vicia faba. *Nanomaterials*, *15*(1), 77. https://doi.org/10.3390/nano15010077

Alolga, R. N., Wang, F., Zhang, X., Li, J., Tran, L.-S. P., & Yin, X. (2022). Bioactive Compounds from the Zingiberaceae Family with Known Antioxidant Activities for Possible Therapeutic Uses. *Antioxidants*, *11*(7), 1281. https://doi.org/10.3390/antiox11071281

Ansar, S., Tabassum, H., Aladwan, N. S. M., Alsubki, R., Abudawood, M., Almahrouqi, S., Naiman Ali, M., Banu, N., & Almaarik, B. (2020). Eco friendly silver nanoparticles synthesis by Brassica oleracea and its antibacterial, anticancer and antioxidant properties. *Scientific Reports*, *10*(1). https://doi.org/10.1038/s41598-020-74371-8

Bahuguna, A., Khan, I., Bajpai, V. K., & Kang, S. C. (2017). MTT assay to evaluate the cytotoxic potential of a drug. *Bangladesh Journal of Pharmacology*, *12*(2). https://doi.org/10.3329/bjp.v12i2.30892

Bélteky, P., Rónavári, A., Igaz, N., Szerencsés, B., Tóth, I. Y., Pfeiffer, I., Kiricsi, M., & Kónya, Z. (2019). Silver nanoparticles: Aggregation behavior in biorelevant conditions and its impact on biological activity. *International Journal of Nanomedicine*, 667–687. https://doi.org/10.2147/IJN.S185965

Bhattacharjee, S. (2016). DLS and zeta potential – What they are and what they are not? *Journal of Controlled Release*, *235*, 337–351. https://doi.org/10.1016/j.jconrel.2016.06.017

Clinical, & Institute, L. S. (2020). Performance standards for antimicrobial susceptibility testing. In: Clinical and laboratory standards institute Wayne, PA.

Danaei, M., Dehghankhold, M., Ataei, S., Hasanzadeh Davarani, F., Javanmard, R., Dokhani, A., Khorasani, S., & Mozafari, M. R. (2018). Impact of Particle Size and Polydispersity Index on the Clinical Applications of Lipidic Nanocarrier Systems. *Pharmaceutics*, *10*(2).

De Mel, S., Gruenler, J., Khoury, L., Heynes, A., Fazekas, J., Damaske, K., Galbadage, T., Gunasekera, R. S., & Anderson, R. S. (2025). Green synthesis of silver nanoparticles using Magnolia alba leaf extracts and evaluating their antimicrobial, anticancer, antioxidant, and photocatalytic properties. *Scientific Reports*, *15*(1), 23709. https://doi.org/10.1038/s41598-025-08468-3

Dutta, T., Das, M., Mandal, V., Chattopadhyay, A. P., Ghosh, N. N., & Mandal, M. (2019). Facile Green Synthesis of Silver Bionanocomposite with Size Dependent Antibacterial and Synergistic Effects: A Combined Experimental and Theoretical Studies. *Journal of Inorganic and Organometallic Polymers and Materials*, *30*(5), 1839–1851. https://doi.org/10.1007/s10904-019-01332-8

Edison, T. J. I., & Sethuraman, M. G. (2012). Instant green synthesis of silver nanoparticles using Terminalia chebula fruit extract and evaluation of their catalytic activity on reduction of methylene blue. *Process Biochemistry*, *47*(9), 1351–1357. https://doi.org/10.1016/j.procbio.2012.04.025

Fahim, M., Shahzaib, A., Nishat, N., Jahan, A., Bhat, T. A., & Inam, A. (2024). Green synthesis of silver nanoparticles: A comprehensive review of methods, influencing factors, and applications. *JCIS Open*, *16*, 100125. https://doi.org/10.1016/j.jciso.2024.100125

Getachew, A. T., Jacobsen, C., Holdt, S. L., & Meyer, A. S. (2022). Effect of Extraction Temperature on Pressurized Liquid Extraction of Bioactive Compounds from Fucus vesiculosus. *Marine Drugs*, *20*(4), 263. https://doi.org/10.3390/md20040263

Gooz, M., & Maldonado, E. N. (2023). Fluorescence microscopy imaging of mitochondrial metabolism in cancer cells [Review]. *Frontiers in Oncology*, *Volume 13 - 2023*. https://doi.org/10.3389/fonc.2023.1152553

Gurunathan, S., Han, J. W., Dayem, A. A., Eppakayala, V., & Kim, J.-H. (2012). Oxidative stress-mediated antibacterial activity of graphene oxide and reduced graphene oxide in Pseudomonas aeruginosa. *International Journal of Nanomedicine*, 5901–5914. https://doi.org/10.2147/IJN.S37397

Ilavenil, K. K., Senthilkumar, V., & Kasthuri, A. (2025). Green synthesis of metal nanoparticles from three medicinal plants: a review of environmental and health applications. *Discover Catalysis*, *2*(1). https://doi.org/10.1007/s44344-025-00007-6

Iravani, S. (2011). Green synthesis of metal nanoparticles using plants [10.1039/C1GC15386B]. *Green Chemistry*, *13*(10), 2638–2650. https://doi.org/10.1039/C1GC15386B

Kaabipour, S., & Hemmati, S. (2021). A review on the green and sustainable synthesis of silver nanoparticles and one-dimensional silver nanostructures. *Beilstein Journal of Nanotechnology*, *12*, 102–136. https://doi.org/10.3762/bjnano.12.9

Le Berre, M., Dziembała, I., Gerlach, J. Q., & Kilcoyne, M. (2022). Calculating Half Maximal Inhibitory Concentration (IC50) Values from Glycomics Microarray Data Using GraphPad Prism. *Methods in molecular biology (Clifton, N.J.)*, *2460*, 89–111. https://doi.org/10.1007/978-1-0716-2148-6_6

Liu, Y., Duan, Y., & Li, W. (2019). Effect of H2O2 induced oxidative stress (OS) on volatile organic compounds (VOCs) and intracellular metabolism in MCF-7 breast cancer cells. *Journal of Breath Research*, *13*(3), 036005. https://doi.org/10.1088/1752-7163/ab14a5

Makarov, V. V., Love, A. J., Sinitsyna, O. V., Makarova, S. S., Yaminsky, I. V., Taliansky, M. E., & Kalinina, N. O. (2014). "Green" Nanotechnologies: Synthesis of Metal Nanoparticles Using Plants. *Acta Naturae*, *6*(1), 35–44. https://doi.org/10.32607/20758251-2014-6-1-35-44

Matyushov, D. V. (2024). Electrophoretic Mobility of Nanoparticles in Water. *The Journal of Physical Chemistry B*, *128*(12), 2930–2938. https://doi.org/10.1021/acs.jpcb.3c08172

Miranda, A., Akpobolokemi, T., Chung, E., Ren, G., & Raimi-Abraham, B. T. (2022). pH Alteration in Plant-Mediated Green Synthesis and Its Resultant Impact on Antimicrobial Properties of Silver Nanoparticles (AgNPs). *Antibiotics*, *11*(11), 1592. https://doi.org/10.3390/antibiotics11111592

More, P. R., Pandit, S., Filippis, A. D., Franci, G., Mijakovic, I., & Galdiero, M. (2023). Silver Nanoparticles: Bactericidal and Mechanistic Approach against Drug Resistant Pathogens. *Microorganisms*, *11*(2), 369. https://doi.org/10.3390/microorganisms11020369

Mosmann, T. (1983). Rapid colorimetric assay for cellular growth and survival: Application to proliferation and cytotoxicity assays. *Journal of Immunological Methods*, *65*(1), 55–63. https://doi.org/10.1016/0022-1759(83)90303-4

Mourdikoudis, S., Pallares, R. M., & Thanh, N. T. K. (2018). Characterization techniques for nanoparticles: comparison and complementarity upon studying nanoparticle properties [10.1039/C8NR02278J]. *Nanoscale*, *10*(27), 12871–12934. https://doi.org/10.1039/C8NR02278J

Murphy, M. P., Bayir, H., Belousov, V., Chang, C. J., Davies, K. J. A., Davies, M. J., Dick, T. P., Finkel, T., Forman, H. J., Janssen-Heininger, Y., Gems, D., Kagan, V. E., Kalyanaraman, B., Larsson, N.-G., Milne, G. L., Nyström, T., Poulsen, H. E., Radi, R., Van Remmen, H.,…Halliwell, B. (2022). Guidelines for measuring reactive oxygen species and oxidative damage in cells and in vivo. *Nature Metabolism*, *4*(6), 651–662. https://doi.org/10.1038/s42255-022-00591-z

Nanda, A., Mohapatra, D. B. B., Mahapatra, A. P. K., Mahapatra, A. P. K., & Mahapatra, A. P. K. (2021). Multiple comparison test by Tukey's honestly significant difference (HSD): Do the confident level control type I error. *International Journal of Statistics and Applied Mathematics*, *6*(1), 59–65. https://doi.org/10.22271/maths.2021.v6.i1a.636

Nargis, M., Ihsan, A. B., & Koyama, Y. (2019). Bolaamphiphilic properties and pH-dependent micellization of quercetin polyglycoside. *RSC Adv*, *9*(58), 33674–33677. https://doi.org/10.1039/c9ra05711k

Nosrati, F., Fakheri, B., Ghaznavi, H., Mahdinezhad, N., Sheervalilou, R., & Fazeli-Nasab, B. (2025). Green synthesis of silver nanoparticles from plant Astragalus fasciculifolius Bioss and evaluating cytotoxic effects on MCF7 human breast cancer cells. *Sci Rep*, *15*(1), 25474. https://doi.org/10.1038/s41598-025-05224-5

Ongtanasup, T., Kamdenlek, P., Manaspon, C., & Eawsakul, K. (2024). Green-synthesized silver nanoparticles from Zingiber officinale extract: antioxidant potential, biocompatibility, anti-LOX properties, and in silico analysis. *BMC Complement Med Ther*, *24*(1), 84. https://doi.org/10.1186/s12906-024-04381-w

Pankey, G. A., & Sabath, L. D. (2004). Clinical Relevance of Bacteriostatic versus Bactericidal Mechanisms of Action in the Treatment of Gram-Positive Bacterial Infections. *Clinical Infectious Diseases*, *38*(6), 864–870. https://doi.org/10.1086/381972

Park, Y., Kim, Y. S., Linhardt, R. J., Weyers, A., & Hong, Y. N. (2011). Polysaccharides and phytochemicals: a natural reservoir for the green synthesis of gold and silver nanoparticles. *IET Nanobiotechnology*, *5*(3), 69–78. https://doi.org/10.1049/iet-nbt.2010.0033

Pugazhendhi, S., Kirubha, E., Palanisamy, P. K., & Gopalakrishnan, R. (2015). Synthesis and characterization of silver nanoparticles from Alpinia calcarata by Green approach and its applications in bactericidal and nonlinear optics. *Applied Surface Science*, *357*, 1801–1808. https://doi.org/10.1016/j.apsusc.2015.09.237

Raza, F., Azad, A., Zafar, H., & Sulaiman, M. (2023). Factors Influencing the Green Synthesis of Metallic Nanoparticles Using Plant Extracts: A Comprehensive Review. *Pharmaceutical Fronts*, *05*(03), e117–e131. https://doi.org/10.1055/s-0043-1774289

Richards, L. A., Dyer, L. A., Forister, M. L., Smilanich, A. M., Dodson, C. D., Leonard, M. D., & Jeffrey, C. S. (2015). Phytochemical diversity drives plant–insect community diversity. *Proceedings of the National Academy of Sciences*, *112*(35), 10973–10978. https://doi.org/10.1073/pnas.1504977112

Sati, A., Ranade, T. N., Mali, S. N., Ahmad Yasin, H. K., & Pratap, A. (2025). Silver Nanoparticles (AgNPs): Comprehensive Insights into Bio/Synthesis, Key Influencing Factors, Multifaceted Applications, and Toxicity-A 2024 Update. *ACS Omega*, *10*(8), 7549–7582. https://doi.org/10.1021/acsomega.4c11045

Sebaugh, J. L. (2011). Guidelines for accurate EC50/IC50 estimation. *Pharmaceutical Statistics*, *10*(2), 128–134. https://doi.org/10.1002/pst.426

Singh, P., Kim, Y.-J., Zhang, D., & Yang, D.-C. (2016). Biological Synthesis of Nanoparticles from Plants and Microorganisms. *Trends in Biotechnology*, *34*(7), 588–599. https://doi.org/10.1016/j.tibtech.2016.02.006

Singh, P., Thygesen, A., Sultan, A., Mateiu, R. V., Pandit, S., Mackevica, A., Baun, A., Mijakovic, I., Daugaard, A. E., Garnæs, J., Tunjic, S., & Mokkapati, V. (2018). Green synthesis of gold and silver nanoparticles from Cannabis sativa (industrial hemp) and their capacity for biofilm inhibition. *International Journal of Nanomedicine*, *13*(7), 3571–3591. https://doi.org/10.2147/ijn.s157958

Smith, M. C., McNeil, S. E., Crist, R. M., & Clogston, J. D. (2017). Zeta potential: a case study of cationic, anionic, and neutral liposomes. *Analytical and Bioanalytical Chemistry*, *409*(24), 5779–5787. https://doi.org/10.1007/s00216-017-0527-z

Souza, T. G. F., Ciminelli, V. S. T., & Mohallem, N. D. S. (2016). A comparison of TEM and DLS methods to characterize size distribution of ceramic nanoparticles. *Journal of Physics: Conference Series*, *733*(1), 012039. https://doi.org/10.1088/1742-6596/733/1/012039

Taherpour, A., Zarban, A., Asadian, A. H., Karbasi, S., & Shakibaie, M. (2025). Efficacy of curcumin-synthesized silver nanoparticles on MCF-7 breast cancer cells. *Med Oncol*, *42*(7), 265. https://doi.org/10.1007/s12032-025-02809-y

Vanlalveni, C., Lallianrawna, S., Biswas, A., Selvaraj, M., Changmai, B., & Rokhum, S. L. (2021). Green synthesis of silver nanoparticles using plant extracts and their antimicrobial activities: a review of recent literature [10.1039/D0RA09941D]. *RSC Advances*, *11*(5), 2804–2837. https://doi.org/10.1039/D0RA09941D

Velmurugan, P., Anbalagan, K., Manosathyadevan, M., Lee, K. J., Cho, M., Lee, S. M., Park, J. H., Oh, S. G., Bang, K. S., & Oh, B. T. (2014). Green synthesis of silver and gold nanoparticles using Zingiber officinale root extract and antibacterial activity of silver nanoparticles against food pathogens. *Bioprocess Biosyst Eng*, *37*(10), 1935–1943. https://doi.org/10.1007/s00449-014-1169-6

Wang, H., & Joseph, J. A. (1999). Quantifying cellular oxidative stress by dichlorofluorescein assay using microplate reader11Mention of a trade name, proprietary product, or specific equipment does not constitute a guarantee by the United States Department of Agriculture and does not imply its approval to the exclusion of other products that may be suitable. *Free Radical Biology and Medicine*, *27*(5), 612–616. https://doi.org/10.1016/S0891-5849(99)00107-0

Wiegand, I., Hilpert, K., & Hancock, R. E. W. (2008). Agar and broth dilution methods to determine the minimal inhibitory concentration (MIC) of antimicrobial substances. *Nature Protocols*, *3*(2), 163–175. https://doi.org/10.1038/nprot.2007.521

Xiao, J., & Högger, P. (2015). Stability of dietary polyphenols under the cell culture conditions: avoiding erroneous conclusions. *J Agric Food Chem*, *63*(5), 1547–1557. https://doi.org/10.1021/jf505514d

Zhou, F., Peterson, T., Fan, Z., & Wang, S. (2023). The Commonly Used Stabilizers for Phytochemical-Based Nanoparticles: Stabilization Effects, Mechanisms, and Applications. *Nutrients*, *15*(18). https://doi.org/10.3390/nu15183881

Zhou, J., Chizhik, A. I., Jin, D., & Chu, S. (2020). Single-particle spectroscopy for functional nanomaterials. *Nature*, *579*(7797), 41–50. https://doi.org/10.1038/s41586-020-2048-8

Zubair, M., & Bokhari, S. (2025). Apoptosis. StatPearls. In: StatPearls Publishing Copyright.

Supplementary Files

This is a list of supplementary files associated with this preprint. Click to download.

- SI.docx